
Article:
Chen, L, Borrelli, R, Shalashilin, DV orcid.org/0000-0001-6104-1277 et al. (2 more authors) (2021) Simulation of Time- and Frequency-Resolved Four-Wave-Mixing Signals at Finite Temperatures: A Thermo-Field Dynamics Approach. Journal of Chemical Theory and Computation. ISSN 1549-9618

https://doi.org/10.1021/acs.jctc.1c00259

Simulation of time- and frequency-resolved four-wave-mixing signals at finite temperature: a thermo-field dynamics approach

Lipeng Chen,[†] Raffaele Borrelli,[‡] Dmitrii V. Shalashilin,[¶] Yang Zhao,[*,§] and Maxim F. Gelin[*,‖]

[†]*Max Planck Institute for the Physics of Complex Systems, Nöthnitzer Str 38, Dresden, Germany*

[‡]*Department of Agricultural, Forestry and Food Science, Università di Torino, I-10095 Grugliasco, TO, Italy*

[¶]*School of Chemistry, University of Leeds, Leeds LS2 9JT, United Kingdom*

[§]*Division of Materials Science, Nanyang Technological University, Singapore 639798, Singapore*

[‖]*School of Science, Hangzhou Dianzi University, Hangzhou 310018, China*

E-mail: YZhao@ntu.edu.sg; maxim@hdu.edu.cn

Abstract

We have proposed a new approach to simulating four-wave-mixing signals of molecular systems at finite temperatures by combining the multiconfigurational Ehrenfest method with the thermo-field dynamics theory. In our approach, the four-time correlation functions at finite temperatures are mapped to those at the zero temperature in an enlarged Hilbert space of twice vibrational degrees of freedom. As an illustration, we have simulated three multidimensional spectroscopic signals, time and frequency-resolved fluorescence spectra, transient-absorption pump-probe spectra, and electronic

2D spectra at finite temperatures, for a conical intersection mediated singlet fission model of the rubrene crystal. It is shown that a detailed dynamical picture of the singlet fission process can be extracted from the three spectroscopic signals. An increasing temperature leads to lower intensities of the signals and broadened vibrational peaks, which can be attributed to faster singlet-triplet population transfer and stronger bath-induced electronic dephasing at higher temperatures.

1 Introduction

With recent technological advances, the technique of multidimensional spectroscopy has been increasingly used to probe energy and charge transfer processes in organic solar cells as well as natural light harvesting complexes[1–4]. Compared to linear spectroscopy in which the spectral lines are often congested, ultrafast non-linear spectroscopic techniques involve many laser interactions allowing for differentiation of dynamical processes with different time responses. The state-of-the-art nonlinear spectroscopies include, among others, fluorescence up-conversion, pump-probe, transient grating, photon echo, which are also referred to as four-wave-mixing (4WM) spectroscopies. Two-dimensional (2D) spectroscopy, in particular, has emerged as a powerful technique in the infrared as well as in the visible spectral range[5,6]. In a 2D spectroscopy experiment, three ultra-short laser pulses, separated by two time delays, namely, the coherence time and the waiting time, are incident on the sample, and the resultant signal field is spectrally resolved in a given phase-matched direction. However, the interpretation of the measured spectroscopic responses in terms of the underlying molecular structure and dynamics is not a trivial task, which necessitates theoretical simulations to extract intrinsic system dynamics encoded from spectroscopic signals.

Simulation of 4WM spectroscopy signals involves the calculation of the third-order polarization $P^{(3)}(t)$[1,7,8]. There exist two alternative groups of theoretical methods for the calculation of $P^{(3)}(t)$. The methods of the first group are based on the nonperturbative evaluation of spectroscopic signals, in which the laser fields are incorporated into the system

Hamiltonian and the dynamics of the driven system is calculated numerically[9,10]. The nonperturbative approach has been combined with multiconfigurational time-dependent Hartree (MCTDH) method[11,12] and quasiclassical mapping Hamiltonian method[13] for the calculation of 4WM spectroscopy signals. A variant of the nonperturbative description of time-resolved spectroscopy, the equation-of-motion phase-matching approach (EOM-PMA), was developed to simulate signals of any order and for any phase-matching direction[8,14]. The alternative, more popular and mature, to the nonperturbative approach is based on the perturbation theory in matter-field interactions, which describes the 4WM signals in terms of third-order nonlinear response functions[7]. The evaluation of the multi-time response functions requires numerical techniques capable of solving coupled multi-dimensional electronic and nuclear dynamics.

A conceptually straightforward framework for simulating third-order polarization is to adopt the density matrix formalism, where nonlinear response functions are obtained by propagating the density matrix of the materials system along different Liouville pathways. The numerically exact approaches of hierarchical equations of motion (HEOM)[15,16] and the quasiadiabatic path integral (QUAPI)[17,18] are two most successful among density matrix methods for computing the nonlinear spectra[19–22]. While both methods eliminate several well-known limitations of the reduced equations-of-motion approaches, including the rotating wave approximation, the white noise (Markovian) approximation, and the perturbative approximant that is associated with the dynamical positivity problem, they are computationally prohibitive in strong system-bath coupling regimes and at very low temperatures. Furthermore, the construction of the HEOM restricts its applications to only certain forms of bath spectral densities, although several spectrum decomposition techniques have been developed to tackle this issue[23–25]. While a large number of numerically efficient approximate methods based on the density matrix formalism have been proposed during past several decades[26–33], the validity of those methods, however, is limited to specific parameter regimes and system dependent.

The wave function-based methods offer an alternative way to compute third-order nonlinear response functions at zero temperature. To solve the time-dependent Schrödinger equation (TDSE), the wave function is expanded in a set of time-dependent basis functions and propagated along the time using certain numerical techniques. The MCTDH method[34,35] and its multilayer version (ML-MCTDH)[36,37] , are among the most popular, powerful wavefunction-based methods, providing an effective tool for accurate simulation of quantum dynamics with many degrees of freedom (DOFs). The Gaussian basis method, in which the nuclear wave packet is expanded with time-dependent Gaussian basis functions, is another promising technique for solving the TDSE. A large body of Gaussian basis methods have been developed in the past years to provide compelling tools for simulating complex molecular systems. They include, among others, the multiple spawning (MS) method[38,39], the coupled coherent states (CCS)[40], the multiconfigurational Ehrenfest (MCE) method[41–43], the method of variational Multiconfigurational Gaussian (vMCG)[44], the hierarchy of the Davydov ansätze (DA)[45–50], and the Gaussian-based MCTDH (G-MCTDH) method[51,52]. It is well known, however, that wavefunction-based methods can be computationally expensive at high temperatures since a large number of statistical samplings for different initial conditions of vibrational modes is required to properly account for the temperature effect[53,54]. A particularly promising technique to mitigate this computational bottleneck is to employ the thermo-field dynamics (TFD)[55,56], a finite temperature representation of quantum mechanics. The method of TFD handles finite-temperature effects by mapping the Liouville-von Neumann equation for the density matrix to the TFD Schrödinger equation with twice as many DOFs, the dynamics of which are then calculated with wave function-based methods. The TFD theory has been applied to treat quantum electron-vibrational dynamics[57–59], finite temperature vibronic spectra[60,61], and finite-temperature electronic structure[62,63].

Recently, we have extended the MCE method to the simulation of 4WM signals at zero temperature by integrating the MCE method into the framework of the nonlinear response functions theory[64]. However, how to extend the MCE method to computing finite-

temperature 4WM signals, a central task of this work, is still an open question to be addressed. Here, we combine the MCE method with the TFD theory in order to introduce temperature effects to nonlinear response functions. We then apply the theory to study spectroscopic signatures of the singlet fission process at finite temperatures in rubrene crystal. The rest of this paper is organized as follows. In Section 2, we describe the model Hamiltonian, the third-order response functions, and the application to a two-state singlet fission model. Simulated 4WM signals are presented and discussed in Section 3. Conclusions are drawn in Section 4.

2 METHODOLOGY

2.1 The model Hamiltonian

We consider a system consisting of an electronic ground state $|g\rangle$ and several electronic excited states $|e\rangle$, $e = 1, 2, \cdots, \mathrm{N_e}$ ($\mathrm{N_e}$ is the number of electronic excited states). The Hamiltonian of the system can be written as

$$\hat{H} = \hat{H}_g + \hat{H}_e \tag{1}$$

with

$$\begin{aligned} \hat{H}_g &= |g\rangle h_g(\hat{\mathbf{q}}, \hat{\mathbf{p}})\langle g|, \\ \hat{H}_e &= \sum_{e,e'}^{\mathrm{N_e}} |e\rangle h_{ee'}(\hat{\mathbf{q}}, \hat{\mathbf{p}})\langle e'| = \sum_{e}^{\mathrm{N_e}} |e\rangle(\epsilon_e + h_e(\hat{\mathbf{q}}, \hat{\mathbf{p}}))\langle e| + \sum_{e\neq e'}^{\mathrm{N_e}} |e\rangle V_{ee'}(\hat{\mathbf{q}})\langle e'| \end{aligned} \tag{2}$$

where $\hat{\mathbf{q}} = \{\hat{\mathbf{q}}_1, \hat{\mathbf{q}}_2, \cdots, \hat{\mathbf{q}}_{\mathrm{N_n}}\}$ and $\hat{\mathbf{p}} = \{\hat{\mathbf{p}}_1, \hat{\mathbf{p}}_2, \cdots, \hat{\mathbf{p}}_{\mathrm{N_n}}\}$ are the mass-weighted coordinates and momenta of $\mathrm{N_n}$ nuclear DOFs. ϵ_e is the vertical excitation energy of the eth electronic excited state. $h_g(\hat{\mathbf{q}}, \hat{\mathbf{p}})$, $h_e(\hat{\mathbf{q}}, \hat{\mathbf{p}})$ are vibrational Hamiltonians of the electronic ground state and eth electronic excited state, respectively, and $V_{ee'}(\hat{\mathbf{q}})$ is the interstate vibrational coupling

Hamiltonian between electronic excited states e and e'. For the ease of derivations in the later section, we further write the vibrational Hamiltonians in terms of creation and annihilation operators.

$$\hat{\mathbf{b}}^\dagger = \frac{\hat{\mathbf{q}} - i\hat{\mathbf{p}}}{\sqrt{2}}, \quad \hat{\mathbf{b}} = \frac{\hat{\mathbf{q}} + i\hat{\mathbf{p}}}{\sqrt{2}}. \tag{3}$$

with $\hat{\mathbf{b}}^\dagger = \left\{\hat{b}_1^\dagger, \hat{b}_2^\dagger, \cdots, \hat{b}_{\mathrm{N_{mod}}}^\dagger\right\}$ and $\hat{\mathbf{b}} = \left\{\hat{b}_1, \hat{b}_2, \cdots, \hat{b}_{\mathrm{N_{mod}}}\right\}$ being the creation and annihilation operators of $\mathrm{N_{mod}}$ normal modes. Employing the harmonic approximation for the ground state potential energy surface (PES), one arrives at

$$\begin{aligned} \hat{h}_g = & \quad \sum_{l}^{\mathrm{N_{mod}}} \hbar\omega_l \hat{b}_l^\dagger \hat{b}_l, \\ \hat{H}_e = & \quad \begin{vmatrix} h_{11}^{\mathrm{ord}}(\hat{\mathbf{b}}^\dagger, \hat{\mathbf{b}}) & h_{12}^{\mathrm{ord}}(\hat{\mathbf{b}}^\dagger, \hat{\mathbf{b}}) & \cdots & h_{1\mathrm{N_e}}^{\mathrm{ord}}(\hat{\mathbf{b}}^\dagger, \hat{\mathbf{b}}) \\ h_{21}^{\mathrm{ord}}(\hat{\mathbf{b}}^\dagger, \hat{\mathbf{b}}) & h_{22}^{\mathrm{ord}}(\hat{\mathbf{b}}^\dagger, \hat{\mathbf{b}}) & \cdots & h_{2\mathrm{N_e}}^{\mathrm{ord}}(\hat{\mathbf{b}}^\dagger, \hat{\mathbf{b}}) \\ \vdots & \vdots & \ddots & \vdots \\ h_{\mathrm{N_e}1}^{\mathrm{ord}}(\hat{\mathbf{b}}^\dagger, \hat{\mathbf{b}}) & h_{\mathrm{N_e}2}^{\mathrm{ord}}(\hat{\mathbf{b}}^\dagger, \hat{\mathbf{b}}) & \cdots & h_{\mathrm{N_eN_e}}^{\mathrm{ord}}(\hat{\mathbf{b}}^\dagger, \hat{\mathbf{b}}) \end{vmatrix} \end{aligned} \tag{4}$$

Here, index "ord" denotes that the creation and annihilation operators are reordered in so-called normal ordering, i.e., the powers of $\hat{\mathbf{b}}^\dagger$ precede those of $\hat{\mathbf{b}}$.

2.2 Third-order response functions

The Hamiltonian describing the interactions of the system with three laser fields is defined in the rotating wave approximation as follows

$$H_L = -\sum_{\alpha=1}^{3} \left(\mathbf{E}_\alpha(\mathbf{r}, t) \cdot \boldsymbol{\mu}_+ + \mathbf{E}_\alpha^*(\mathbf{r}, t) \cdot \boldsymbol{\mu}_-\right), \tag{5}$$

with

$$\mathbf{E}_\alpha(\mathbf{r}, t) = \mathbf{s}_\alpha E_\alpha(t - \tau_\alpha) e^{i\mathbf{k}_\alpha \cdot \mathbf{r} - i\omega_\alpha t}, \tag{6}$$

and

$$\boldsymbol{\mu}_+ = \sum_e^{\mathrm{N_e}} \boldsymbol{\mu}_{eg}|e\rangle\langle g|, \quad \boldsymbol{\mu}_- = \sum_e^{\mathrm{N_e}} \boldsymbol{\mu}_{ge}|g\rangle\langle e|. \tag{7}$$

Here $\mathbf{s}_\alpha$, $E_\alpha(t)$, τ_α, $\mathbf{k}_\alpha$, ω_α denote the polarization, the envelope, the central time, the wave vector, and the frequency of the αth laser pulse, respectively. The arrival times of three pulses are defined as

$$\tau_1 = -T_\mathrm{w} - \tau, \quad \tau_2 = -T_\mathrm{w}, \quad \tau_3 = 0, \tag{8}$$

where τ is the delay time between the second and the first pulse, and T_w (also called population time) is the delay time between the third and the second pulse. The transition dipole moment operator is defined as $\boldsymbol{\mu} = \boldsymbol{\mu}_+ + \boldsymbol{\mu}_-$ with $\boldsymbol{\mu}_+$ and $\boldsymbol{\mu}_-$ being the up and down transition dipole moment operator, respectively.

The simulation of 4WM signals involves the calculation of third-order nonlinear response functions. The four third-order response functions R_a, $a = 1, 2, 3, 4$, are expressed in terms of four-time correlation functions of the transition dipole moment operators as[7]

$$\begin{aligned}
R_1(t_3, t_2, t_1) &= \Phi(t_1, t_1 + t_2, t_1 + t_2 + t_3, 0), \\
R_2(t_3, t_2, t_1) &= \Phi(0, t_1 + t_2, t_1 + t_2 + t_3, t_1), \\
R_3(t_3, t_2, t_1) &= \Phi(0, t_1, t_1 + t_2 + t_3, t_1 + t_2), \\
R_4(t_3, t_2, t_1) &= \Phi(t_1 + t_2 + t_3, t_1 + t_2, t_1, 0).
\end{aligned} \tag{9}$$

with

$$\Phi\left(\tau_4, \tau_3, \tau_2, \tau_1\right) = \langle \boldsymbol{\mu}_-(\tau_4)\boldsymbol{\mu}_+(\tau_3)\boldsymbol{\mu}_-(\tau_2)\boldsymbol{\mu}_+(\tau_1)\rangle \tag{10}$$

where $\boldsymbol{\mu}_\pm(\tau)$ denotes the Heisenberg representation of $\boldsymbol{\mu}_\pm$, i.e., $\boldsymbol{\mu}_\pm(\tau) = e^{iH\tau}\boldsymbol{\mu}_\pm e^{-iH\tau}$. In Eq. 10, the angular brackets represent the trace over vibrational and electronic DOFs. The

four-time correlation function (Eq. 10) can be written explicitly as

$$\Phi(\tau_4,\tau_3,\tau_2,\tau_1) = \mathrm{Tr}\left(\hat{\rho}_g\langle g|e^{i\hat{h}_g\tau_4}\boldsymbol{\mu}_- e^{-i\hat{H}_e(\tau_4-\tau_3)}\boldsymbol{\mu}_+ e^{-i\hat{h}_g(\tau_3-\tau_2)}\boldsymbol{\mu}_- e^{-i\hat{H}_e(\tau_2-\tau_1)}\boldsymbol{\mu}_+ e^{-i\hat{h}_g\tau_1}|g\rangle\right) \tag{11}$$

where

$$\hat{\rho}_g = Z_g^{-1}\exp\left\{-\beta\hat{h}_g\right\} \tag{12}$$

is the density matrix of the vibrational DOFs at temperature T. Here, $Z_g = \mathrm{Tr}\left(e^{-\beta\hat{h}_g}\right)$ is the partition function, $\beta = (k_\mathrm{B}T)^{-1}$, and k_B is the Boltzmann constant.

2.2.1 Zero temperature

At zero temperature, the four-time correlation function (Eq. 11) can be further simplified as

$$\Phi(\tau_4,\tau_3,\tau_2,\tau_1) = \langle g|_g\langle 0|\boldsymbol{\mu}_- e^{-i\hat{H}_e(\tau_4-\tau_3)}\boldsymbol{\mu}_+ e^{-i\hat{h}_g(\tau_3-\tau_2)}\boldsymbol{\mu}_- e^{-i\hat{H}_e(\tau_2-\tau_1)}\boldsymbol{\mu}_+|0\rangle_g|g\rangle \tag{13}$$

In the derivation, we have used the fact that in the zero temperature limit, $\hat{\rho}_g = |0\rangle_{gg}\langle 0|$ and $e^{-i\hat{h}_g t}|0\rangle_g = |0\rangle_g$ (for convenience, the total zero-point vibrational energy is set to zero).

2.2.2 Finite temperature

At non-zero temperatures, we demonstrate that the evaluation of the four-time correlation function (Eq. 11) can be done in a same way as in the zero-temperature case by employing the TFD formalism.

Following the TFD, we first express the expectation value of any operator $\hat{Q}$ in the vibrational space in terms of a "thermal vacuum state" $|\mathbf{0}(\beta)\rangle$ [55,56]

$$\langle\hat{Q}\rangle = \mathrm{Tr}\left\{\hat{\rho}_g\hat{Q}\right\} = \langle\mathbf{0}(\beta)|\hat{Q}|\mathbf{0}(\beta)\rangle, \tag{14}$$

where $|\mathbf{0}(\beta)\rangle$ is the temperature-dependent "vacuum state" defined as[56]

$$\begin{aligned} |\mathbf{0}(\beta)\rangle &= Z_g^{-1/2} \sum_l e^{-\beta\hbar\omega_l/2} |l, \tilde{l}\rangle \\ &= Z_g^{-1/2} e^{-\frac{1}{2}\beta\hat{h}_g} |\boldsymbol{I}\rangle; \quad |\boldsymbol{I}\rangle = \sum_l |l, \tilde{l}\rangle. \end{aligned} \tag{15}$$

Here $|l\rangle$ is the eigenstate of the vibrational Hamiltonian $\hat{h}_g$ with eigenvalue $\hbar\omega_l$, and $|\tilde{l}\rangle$ is the eigenstate of the corresponding fictitious Hamiltonian $\hat{\tilde{h}}_g = \sum_l \hbar\omega_l \hat{\tilde{b}}_l^\dagger \hat{\tilde{b}}_l$. We can thus rewrite Eq. 11 as

$$\Phi(\tau_4, \tau_3, \tau_2, \tau_1) = \langle g|\langle \mathbf{0}(\beta)| e^{i\hat{h}_g\tau_4} \boldsymbol{\mu}_- e^{-i\hat{H}_e(\tau_4-\tau_3)} \boldsymbol{\mu}_+ e^{-i\hat{h}_g(\tau_3-\tau_2)} \boldsymbol{\mu}_- e^{-i\hat{H}_e(\tau_2-\tau_1)} \boldsymbol{\mu}_+ e^{-i\hat{h}_g\tau_1} |\mathbf{0}(\beta)\rangle |g\rangle \tag{16}$$

Eq. 16 can be further recast as

$$\Phi(\tau_4, \tau_3, \tau_2, \tau_1) = \langle g|\langle \mathbf{0}(\beta)| \boldsymbol{\mu}_- e^{-i(\hat{H}_e-\hat{\tilde{h}}_g)(\tau_4-\tau_3)} \boldsymbol{\mu}_+ e^{-i(\hat{h}_g-\hat{\tilde{h}}_g)(\tau_3-\tau_2)} \boldsymbol{\mu}_- e^{-i(\hat{H}_e-\hat{\tilde{h}}_g)(\tau_2-\tau_1)} \boldsymbol{\mu}_+ |\mathbf{0}(\beta)\rangle |g\rangle \tag{17}$$

The reader is referred to Appendix A for a detailed derivation.

It is convenient to express $|\mathbf{0}(\beta)\rangle$ as[56]

$$|\mathbf{0}(\beta)\rangle = e^{-i\hat{G}} |\mathbf{0}\rangle_g, \tag{18}$$

where $|\mathbf{0}\rangle_g = |0\tilde{0}\rangle_g$ is the ground state of the augmented vibrational Hamiltonian ($\hat{h}_g$ and $\hat{\tilde{h}}_g$), and $\hat{G}$ is the Bogoliubov unitary transformation operator defined as

$$\hat{G} = \hat{G}^\dagger = -i \sum_l \theta_l \left(\hat{b}_l \hat{\tilde{b}}_l - \hat{b}_l^\dagger \hat{\tilde{b}}_l^\dagger \right) \tag{19}$$

with

$$\theta_l = \operatorname{arctanh}(e^{-\beta\hbar\omega_l/2}). \tag{20}$$

By substituting Eq. 18 into Eq. 17, we finally obtain

$$\Phi(\tau_4,\tau_3,\tau_2,\tau_1) = \langle g|_g\langle \mathbf{0}|\boldsymbol{\mu}_- e^{-i\hat{\bar{H}}_{e\theta}(\tau_4-\tau_3)}\boldsymbol{\mu}_+ e^{-i\hat{\bar{h}}_{g\theta}(\tau_3-\tau_2)}\boldsymbol{\mu}_- e^{-i\hat{\bar{H}}_{e\theta}(\tau_2-\tau_1)}\boldsymbol{\mu}_+|\mathbf{0}\rangle_g|g\rangle, \tag{21}$$

where we have defined

$$\begin{aligned} \hat{\bar{h}}_{g\theta} &= e^{i\hat{G}}\left(\hat{h}_g - \hat{\bar{h}}_g\right)e^{-i\hat{G}}, \\ \hat{\bar{H}}_{e\theta} &= e^{i\hat{G}}\left(\hat{H}_e - \hat{\bar{h}}_g\right)e^{-i\hat{G}}. \end{aligned} \tag{22}$$

The specific forms of $\hat{\bar{h}}_{g\theta}$ and $\hat{\bar{H}}_{e\theta}$ can be easily derived by using the following relations[56]

$$\begin{aligned} e^{i\hat{G}}\hat{b}_l e^{-i\hat{G}} &= \hat{b}_l\cosh(\theta_l) + \hat{\bar{b}}_l^\dagger\sinh(\theta_l), \\ e^{i\hat{G}}\hat{\bar{b}}_l e^{-i\hat{G}} &= \hat{\bar{b}}_l\cosh(\theta_l) + \hat{b}_l^\dagger\sinh(\theta_l), \\ e^{i\hat{G}}\left(\hat{b}_l^\dagger\hat{b}_l - \hat{\bar{b}}_l^\dagger\hat{\bar{b}}_l\right)e^{-i\hat{G}} &= \hat{b}_l^\dagger\hat{b}_l - \hat{\bar{b}}_l^\dagger\hat{\bar{b}}_l. \end{aligned} \tag{23}$$

Comparing Eqs. 13 and 21, it is found that the four-time correlation function at finite temperatures can be viewed as the zero-temperature correlation function with $\hat{H}_e$, $\hat{h}_g$, and $|0\rangle_g$ substituted by $\hat{\bar{H}}_{e\theta}$, $\hat{\bar{h}}_{g\theta}$, and $|\mathbf{0}\rangle_g$, respectively. The explicit expressions for the four

response functions R_a, $a = 1, 2, 3, 4$, can be obtained from Eq. 21, yielding

$$
\begin{aligned}
& R_1(\tau, T_\mathrm{w}, t) \\
= & \sum_{e_1,e_2,e_3,e_4} \left(\mathbf{s}_4^* \cdot \boldsymbol{\mu}_{ge_3}\right) \left(\mathbf{s}_1 \cdot \boldsymbol{\mu}_{e_4g}\right) \left(\mathbf{s}_2^* \cdot \boldsymbol{\mu}_{ge_1}\right) \left(\mathbf{s}_3 \cdot \boldsymbol{\mu}_{e_2g}\right)_g \langle \mathbf{0}| \langle e_1| e^{i\hat{\tilde{H}}_{e\theta} T_\mathrm{w}} |e_2\rangle e^{i\hat{\tilde{h}}_{g\theta} t} \langle e_3| e^{-i\hat{\tilde{H}}_{e\theta}(\tau + T_\mathrm{w} + t)} |e_4\rangle |\mathbf{0}\rangle_g \\
& R_2(\tau, T_\mathrm{w}, t) \\
= & \sum_{e_1,e_2,e_3,e_4} \left(\mathbf{s}_4^* \cdot \boldsymbol{\mu}_{ge_3}\right) \left(\mathbf{s}_1^* \cdot \boldsymbol{\mu}_{ge_1}\right) \left(\mathbf{s}_2 \cdot \boldsymbol{\mu}_{e_4g}\right) \left(\mathbf{s}_3 \cdot \boldsymbol{\mu}_{e_2g}\right)_g \langle \mathbf{0}| \langle e_1| e^{i\hat{\tilde{H}}_{e\theta}(T_\mathrm{w} + \tau)} |e_2\rangle e^{i\hat{\tilde{h}}_{g\theta} t} \langle e_3| e^{-i\hat{\tilde{H}}_{e\theta}(T_\mathrm{w} + t)} |e_4\rangle |\mathbf{0}\rangle_g \\
& R_3(\tau, T_\mathrm{w}, t) \\
= & \sum_{e_1,e_2,e_3,e_4} \left(\mathbf{s}_4^* \cdot \boldsymbol{\mu}_{ge_3}\right) \left(\mathbf{s}_1^* \cdot \boldsymbol{\mu}_{ge_1}\right) \left(\mathbf{s}_2 \cdot \boldsymbol{\mu}_{e_2g}\right) \left(\mathbf{s}_3 \cdot \boldsymbol{\mu}_{e_4g}\right)_g \langle \mathbf{0}| \langle e_1| e^{i\hat{\tilde{H}}_{e\theta} \tau} |e_2\rangle e^{i\hat{\tilde{h}}_{g\theta}(T_\mathrm{w} + t)} \langle e_3| e^{-i\hat{\tilde{H}}_{e\theta} t} |e_4\rangle |\mathbf{0}\rangle_g \\
& R_4(\tau, T_\mathrm{w}, t) \\
= & \sum_{e_1,e_2,e_3,e_4} \left(\mathbf{s}_4^* \cdot \boldsymbol{\mu}_{ge_1}\right) \left(\mathbf{s}_1 \cdot \boldsymbol{\mu}_{e_4g}\right) \left(\mathbf{s}_2^* \cdot \boldsymbol{\mu}_{ge_3}\right) \left(\mathbf{s}_3 \cdot \boldsymbol{\mu}_{e_2g}\right)_g \langle \mathbf{0}| \langle e_1| e^{-i\hat{\tilde{H}}_{e\theta} t} |e_2\rangle e^{-i\hat{\tilde{h}}_{g\theta} T_\mathrm{w}} \langle e_3| e^{-i\hat{\tilde{H}}_{e\theta} \tau} |e_4\rangle |\mathbf{0}\rangle_g
\end{aligned} \tag{24}
$$

2.3 Application to a linear vibronic coupling model of the singlet fission in crystalline rubrene

In this work, we consider a linear vibronic coupling model of singlet fission (SF) in crystalline rubrene, which was used to study the effect of conical intersections (CIs) in the SF process[65–68]. The model consists of an electronic ground state $|g\rangle$ and two lowest electronic excited states $|\mathrm{S}_1\rangle$ and $|\mathrm{TT}\rangle$, where S_1 and TT are the (optically bright) singlet state and (optically dark) correlated triplet pair state, respectively. The total Hamiltonian ($\hat{H}$) is partitioned into the system Hamiltonian ($\hat{H}_S$), the bath Hamiltonian ($\hat{H}_B$) and their coupling ($\hat{H}_{SB}$)

$$
\hat{H} = \hat{H}_S + \hat{H}_B + \hat{H}_{SB} \tag{25}
$$

In the diabatic representation, the system Hamiltonian $\hat{H}_S$ is written as

$$\begin{aligned}
\hat{H}_S = \quad & |g\rangle\hat{h}_g\langle g| + \sum_{e=\mathrm{S}_1,\mathrm{TT}} |e\rangle(\epsilon_e + \hat{h}_e)\langle e| + (|\mathrm{S}_1\rangle\langle \mathrm{TT}| + |\mathrm{TT}\rangle\langle \mathrm{S}_1|)\lambda\hat{Q}_c \\
\hat{h}_e = \quad & \hat{h}_g + \sum_{m=t} \kappa_m^{(e)}\hat{Q}_m \\
\hat{h}_g = \quad & \frac{1}{2}\sum_{j=c,t} \hbar\Omega_j \left\{\hat{P}_j^2 + \hat{Q}_j^2\right\}
\end{aligned} \tag{26}$$

Here, $\hat{Q}_j$, $\hat{P}_j$ and Ω_j are the dimensionless coordinate, momentum and frequency of the coupling mode (subscript c) and the tuning modes (subscript t), respectively. ϵ_{S_1} and ϵ_{TT} are the vertical excitation energies of S_1 and TT states, respectively. $\kappa_m^{(e)}$ ($e = \mathrm{S}_1, \mathrm{TT}$) are the intra-state electron-vibrational coupling constants of tuning modes, and λ is the inter-state coupling constant of the coupling mode. The values of model parameters are listed in Table 1.

Table 1: Vertical excitation energies ϵ_e (eV), intrastate electron-vibrational coupling constants κ (eV), interstate electronic coupling constant λ (eV), vibrational frequencies Ω (eV) and periods $\tau = 2\pi/\Omega$ (fs).

	S_1	TT	Ω	$\tau = 2\pi/\Omega$
ϵ_e	2.58	2.5812		
κ_{t_1}	0.3720	-0.3720	0.1860	22.2
κ_{t_2}	0.0745	-0.0745	0.0260	159.1
κ_c	0	0	0.0154	268.6
		$\lambda = 0.05$		

After including the primary vibrational modes into the system Hamiltonian, the effect of the remaining intra- and inter- molecular vibrational modes can be described as a bath which consists of a collection of harmonic oscillators

$$\hat{H}_B = \sum_n \frac{1}{2}\hbar\omega_n \left\{\hat{p}_n^2 + \hat{q}_n^2\right\} \tag{27}$$

where $\hat{p}_n$, $\hat{q}_n$ and ω_n are the dimensionless momentum, coordinate, and frequency of the nth

bath oscillators, respectively.

The system-bath coupling Hamiltonian reads

$$\hat{H}_{SB} = \sum_{e=\mathrm{S_1,TT}} |e\rangle(\sum_n \kappa_n^{(e)} \hat{q}_n)\langle e| \tag{28}$$

with $\kappa_n^{(e)}$ being the system-bath coupling constants. For simplicity, we assume that $\kappa_n^{(\mathrm{S_1})} = \kappa_n^{(\mathrm{TT})} = \kappa_n$ in this work. The coupling strength κ_n is fully characterized by the bath spectral density

$$J(\omega) = \frac{\pi}{2} \sum_n \kappa_n^2 \delta(\omega - \omega_n) = \frac{\pi}{2} \eta\omega \exp(-\omega/\omega_c) \tag{29}$$

Here, an Ohmic spectral density is used, with η and ω_c denoting the system-bath coupling strength and the cutoff frequency, respectively. In this work, we use $\eta = 1.0$ and $\omega_c = 800\mathrm{cm}^{-1}$. We then follow the spectral density discretization procedure as described in Refs.[69,70] to obtain κ_n, where the spectral density is divided into $\mathrm{N_b}$ effective modes in the range of $[0, \omega_{\max}]$ with $\omega_{\max} = 4\omega_c$ being the upper bound of the frequency. The frequency and coupling strength of nth bath mode are then expressed by

$$\begin{aligned} \omega_n &= -\omega_c \ln\left(1 - n\frac{\omega_0}{\omega_c}\right), \\ \kappa_n &= \sqrt{2\eta\omega_n\omega_0} \end{aligned} \tag{30}$$

with $\omega_0 = \omega_c \left(1 - e^{-\omega_{\max}/\omega_c}\right)/N_b$.

Using the creation and annihilation operators of normal modes, the total Hamiltonian $\hat{H}$

can be rewritten as

$$
\begin{aligned}
\hat{H} = \quad & |g\rangle\hat{h}_g\langle g| + \hat{H}_e, \\
\hat{h}_g = \quad & \sum_{l}^{\mathrm{N_{mod}}} \hbar\omega_l \hat{b}_l^\dagger \hat{b}_l, \\
\hat{H}_e = \quad & \sum_{e}^{\mathrm{S_1,TT}} \epsilon_e |e\rangle\langle e| + \sum_{l}^{\mathrm{N_{mod}}} \hbar\omega_l \hat{b}_l^\dagger \hat{b}_l + \frac{1}{\sqrt{2}} \sum_{e\neq e'}^{\mathrm{S_1,TT}} \lambda |e\rangle\langle e'|(\hat{b}_c^\dagger + \hat{b}_c) \\
& + \frac{1}{\sqrt{2}} \sum_{e}^{\mathrm{S_1,TT}} \sum_{l\neq c}^{\mathrm{N_{mod}}} \kappa_l^{(e)} |e\rangle\langle e|(\hat{b}_l^\dagger + \hat{b}_l)
\end{aligned} \tag{31}
$$

Here, l labels the 3 primary system modes plus $\mathrm{N_b}$ bath modes ($\mathrm{N_{mod}} = 3 + \mathrm{N_b}$).

In order to calculate 4WM signals at finite temperatures, we need to specify $\hat{\tilde{h}}_{g\theta}$ and $\hat{\tilde{H}}_{e\theta}$ (Eq. 22). The explicit forms of $\hat{\tilde{h}}_{g\theta}$ and $\hat{\tilde{H}}_{e\theta}$ can be derived as

$$
\begin{aligned}
\hat{\tilde{h}}_{g\theta} = \quad & e^{i\hat{G}}(\hat{h}_g - \hat{\tilde{h}}_g)e^{-i\hat{G}} \\
= \quad & \sum_{l}^{\mathrm{N_{mod}}} \hbar\omega_l (\hat{b}_l^\dagger \hat{b}_l - \hat{\tilde{b}}_l^\dagger \hat{\tilde{b}}_l) \\
\hat{\tilde{H}}_{e\theta} = \quad & e^{i\hat{G}}(\hat{H}_e - \hat{\tilde{h}}_g)e^{-i\hat{G}} \\
= \quad & \sum_{e}^{\mathrm{S_1,TT}} \epsilon_e |e\rangle\langle e| + \sum_{l}^{\mathrm{N_{mod}}} \hbar\omega_l (\hat{b}_l^\dagger \hat{b}_l - \hat{\tilde{b}}_l^\dagger \hat{\tilde{b}}_l) + \frac{1}{\sqrt{2}} \sum_{e\neq e'}^{\mathrm{S_1,TT}} \lambda |e\rangle\langle e'| \left\{ (\hat{b}_c^\dagger + \hat{b}_c)\cosh(\theta_c) + (\hat{\tilde{b}}_c^\dagger + \hat{\tilde{b}}_c)\sinh(\theta_c) \right\} \\
& + \frac{1}{\sqrt{2}} \sum_{e}^{\mathrm{S_1,TT}} \sum_{l\neq c} \kappa_l^{(e)} |e\rangle\langle e| \left\{ (\hat{b}_l^\dagger + \hat{b}_l)\cosh(\theta_l) + (\hat{\tilde{b}}_l^\dagger + \hat{\tilde{b}}_l)\sinh(\theta_l) \right\}
\end{aligned} \tag{32}
$$

The expressions of $\hat{\tilde{h}}_{g\theta}$ and $\hat{\tilde{H}}_{e\theta}$ can be further simplified as

$$
\begin{aligned}
\hat{\tilde{h}}_{g\theta} = \quad & \sum_{l}^{\mathrm{2N_{mod}}} \hbar\omega_l' \hat{b}_l'^\dagger \hat{b}_l', \\
\hat{\tilde{H}}_{e\theta} = \quad & \sum_{e}^{\mathrm{S_1,TT}} \epsilon_e |e\rangle\langle e| + \sum_{l}^{\mathrm{2N_{mod}}} \hbar\omega_l' \hat{b}_l'^\dagger \hat{b}_l' + \frac{1}{\sqrt{2}} \sum_{e\neq e'}^{\mathrm{S_1,TT}} \sum_{l}^{\mathrm{2N_{mod}}} |e\rangle\langle e'|\lambda_l'(\hat{b}_l'^\dagger + \hat{b}_l') \\
& + \frac{1}{\sqrt{2}} \sum_{e}^{\mathrm{S_1,TT}} \sum_{l}^{\mathrm{2N_{mod}}} \kappa_l'^{(e)} |e\rangle\langle e|(\hat{b}_l'^\dagger + \hat{b}_l')
\end{aligned} \tag{33}
$$

by introducing the following notations

$$
\begin{aligned}
\hat{b}_l^{'\dagger}(\hat{b}_l^{'}) &= \begin{cases} \hat{b}_l^{\dagger}(\hat{b}_l) & 1 \le l \le \mathrm{N_{mod}} \\ \hat{\tilde{b}}_{l-\mathrm{N_{mod}}}^{\dagger}(\hat{\tilde{b}}_{l-\mathrm{N_{mod}}}) & 1+\mathrm{N_{mod}} \le l \le 2\mathrm{N_{mod}} \end{cases} \\
\omega_l^{'} &= \begin{cases} \omega_l & 1 \le l \le \mathrm{N_{mod}} \\ -\omega_{l-\mathrm{N_{mod}}} & 1+\mathrm{N_{mod}} \le l \le 2\mathrm{N_{mod}} \end{cases} \\
\lambda_l^{'} &= \begin{cases} \lambda_l \cosh(\theta_l) & 1 \le l \le \mathrm{N_{mod}} \\ \lambda_{l-\mathrm{N_{mod}}} \sinh(\theta_{l-\mathrm{N_{mod}}}) & 1+\mathrm{N_{mod}} \le l \le 2\mathrm{N_{mod}} \end{cases} \\
\kappa_l^{'(e)} &= \begin{cases} \kappa_l^{(e)} \cosh(\theta_l) & 1 \le l \le \mathrm{N_{mod}} \\ \kappa_{l-\mathrm{N_{mod}}}^{(e)} \sinh(\theta_{l-\mathrm{N_{mod}}}) & 1+\mathrm{N_{mod}} \le l \le 2\mathrm{N_{mod}} \end{cases}
\end{aligned} \tag{34}
$$

We then substitute the propagators in the four response functions R_a, $a = 1, 2, 3, 4$ (Eq. 24) by the following wave function of the MCE method[41],

$$
\begin{aligned}
e^{-i\hat{\tilde{H}}_{e\theta}t}|e\rangle|\mathbf{0}\rangle_g = & \quad |\Psi(t)\rangle \\
= & \quad \sum_{u=1}^{M} \left(\sum_{e}^{\mathrm{S_1,TT}} A_{ue}(t)|e\rangle \right) |\mathbf{z}_u(t)\rangle \\
= & \quad \sum_{u=1}^{M} \left(\sum_{e}^{\mathrm{S_1,TT}} A_{ue}(t)|e\rangle \right) \exp\left[\sum_{l}^{2\mathrm{N_{mod}}} \left(z_{ul}(t)\hat{b}_l^{'\dagger} - z_{ul}^{*}(t)\hat{b}_l^{'} \right) \right] |\mathbf{0}\rangle_g
\end{aligned} \tag{35}
$$

Here, u is the index for the configuration. A_{ue} is the amplitude in the diabatic electronic excited state $|e\rangle$, and $\mathbf{z}_u$ is the coherent state for the vibrational DOFs. z_{ul} is the phonon displacement for the lth normal mode. In principle, one can apply the Lagrangian formalism of the Dirac-Frenkel variational method to obtain the equations of motion for both state amplitude A_{ue} and phonon displacement u_{ul}. In the MCE method, the variational principle is applied only to A_{ue}, while each $\mathbf{z}_u$ follows its own Ehrenfest trajectory. The reader is referred to the Appendix B for details on the MCE method and its applications to the

calculation of four response functions R_a, $a = 1, 2, 3, 4$.

Following the procedure described in Ref.[71], the initial values of the state amplitudes A_{ue} are obtained from the quantum superposition sampling. The initial values of the phonon displacements z_{ul} (both the real and imaginary part) are sampled from the uniform distribution $[-\delta, \delta]$. Adopting the idea of "compressed pancakes" sampling technique of Shalashilin and Child[72], we use a larger value of $\delta = 5 \times 10^{-2}$ for the primary system modes and a smaller value of $\delta = 10^{-2}$ for bath modes. A configuration of $M = 800$ and $\mathrm{N_b} = 30$ discretized bath modes are employed to achieve high accuracy and efficiency in the calculations of 4WM signals. The transition dipole moments are set as $\mu_{\mathrm{S}_1 g} = 1$ and $\mu_{\mathrm{TT}g} = 0$ since the TT state is optically dark. To account for additional optical dephasing, we further multiply the response functions $R_a(\tau, \mathrm{T_w}, t)$, $a = 1, 2, 3, 4$ (Eq. 24) by $\exp\{-(\tau + t)/\tau_d\}$ with a dephasing time $\tau_d = 80$ fs.

Since higher-lying singlet and triplet states are not included in our model, the third-order polarization $P^{(3)}(t)$ consists of contributions from the stimulated emission (SE) and the ground state bleaching (GSB). While the SE is described by response functions R_1 and R_2 (the system evolves in the electronic excited states during $\mathrm{T_w}$), the GSB is characterized by response functions R_3 and R_4 (the system evolves in the electronic ground state during $\mathrm{T_w}$).

2D electronic spectroscopy is a typical 4WM technique used to study the ultrafast energy relaxation processes in molecular systems. To simulate 2D electronic spectra, we need to decompose $P^{(3)}(t)$ into rephasing (subscript R) and nonrephasing (subscript NR) contributions, which can be written as

$$P^{(3)}(\tau, T_\mathrm{w}, t) = P^{(3)}_\mathrm{R}(\tau, T_\mathrm{w}, t) + P^{(3)}_\mathrm{NR}(\tau, T_\mathrm{w}, t) \tag{36}$$

where in the impulsive limit (when the pulse envelopes can be replaced by the Dirac delta

functions)

$$\begin{aligned} P_{\mathrm{R}}^{(3)}(\tau, T_{\mathrm{w}}, t) \quad &\sim -i\left[R_2(\tau, T_{\mathrm{w}}, t) + R_3(\tau, T_{\mathrm{w}}, t)\right], \\ P_{\mathrm{NR}}^{(3)}(\tau, T_{\mathrm{w}}, t) \quad &\sim -i\left[R_1(\tau, T_{\mathrm{w}}, t) + R_4(\tau, T_{\mathrm{w}}, t)\right]. \end{aligned} \tag{37}$$

2D electronic spectrum is then obtained by 2D Fourier transforms, yielding

$$\begin{aligned} S_{\mathrm{R}}(\omega_\tau, T_{\mathrm{w}}, \omega_t) = \quad & \mathrm{Re}\int_0^\infty \int_0^\infty dt d\tau i P_{\mathrm{R}}^{(3)}(\tau, T_{\mathrm{w}}, t) e^{-i\omega_\tau \tau + i\omega_t t} \\ S_{\mathrm{NR}}(\omega_\tau, T_{\mathrm{w}}, \omega_t) = \quad & \mathrm{Re}\int_0^\infty \int_0^\infty dt d\tau i P_{\mathrm{NR}}^{(3)}(\tau, T_{\mathrm{w}}, t) e^{i\omega_\tau \tau + i\omega_t t} \end{aligned} \tag{38}$$

The total 2D signal is the sum of the above two contributions

$$S(\omega_\tau, T_{\mathrm{w}}, \omega_t) = S_{\mathrm{R}}(\omega_\tau, T_{\mathrm{w}}, \omega_t) + S_{\mathrm{NR}}(\omega_\tau, T_{\mathrm{w}}, \omega_t) \tag{39}$$

The transient absorption (TA) pump-probe spectrum corresponds to the case where $\mathbf{k}_1 = \mathbf{k}_2 = \mathbf{k}_{\mathrm{pump}}$, $\mathbf{k}_3 = \mathbf{k}_{\mathrm{probe}}$ and the signal is detected in the direction of $\mathbf{k}_{\mathrm{probe}}$. In the ultrashort pulse approximation, the TA polarization can be written as

$$P_{\mathrm{TA}}(\mathrm{T_w}, t) \sim -i\left[R_1(0, T_{\mathrm{w}}, t) + R_2(0, T_{\mathrm{w}}, t) + R_3(0, T_{\mathrm{w}}, t) + R_4(0, T_{\mathrm{w}}, t)\right]. \tag{40}$$

The dispersed TA spectrum is obtained by performing the Fourier transform with respect to $P_{\mathrm{TA}}(\mathrm{T_w}, t)$,

$$S_{\mathrm{TA}}(T_{\mathrm{w}}, \omega_t) = \mathrm{Re}\int_0^\infty dt i P_{\mathrm{TA}}(T_{\mathrm{w}}, t) e^{i\omega_t t}. \tag{41}$$

The time and frequency-gated (TFG) fluorescence spectroscopy is a valuable tool for monitoring the wave packet dynamics in the electronic excited states. The TFG signal can be calculated as[73,74]

$$S_{\mathrm{TFG}}(T_{\mathrm{w}}, \omega_t) \sim \mathrm{Re}\int_0^\infty dt_2 dt R_2(0, t_2, t) e^{i\omega_t t} E_f(t + t_2 - T_{\mathrm{w}}) E_f(t_2 - T_{\mathrm{w}}), \tag{42}$$

where $E_f(t)$ denotes the envelop of the gate pulse, assumed to be of Gaussian shape $E_f(t) = \exp\{-(t/\tau_f)^2\}$. Here τ_f is the pulse duration which controls the time resolution of the signal.

3 Results and Discussions

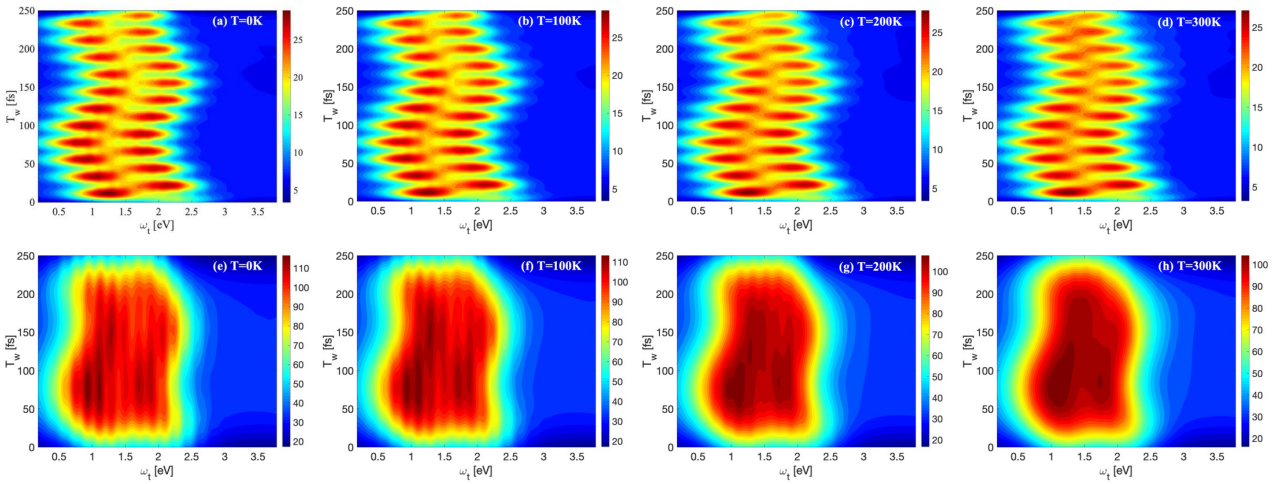

Figure 1: TFG fluorescence spectra $S_{\mathrm{TFG}}(\mathrm{T_w}, \omega_t)$ at different temperatures T=0K, 100K, 200K, and 300K. Upper and lower panels correspond to the cases of good time resolution (τ_f =12 fs) and good frequency resolution (τ_f= 60 fs), respectively.

TFG fluorescence spectroscopy characterizes the wave packet dynamics in the electronic excited states, providing a connection between the electronic population and vibrational wave-packet motions[73–75]. Fig. 1 plots the TFG fluorescence spectra $S_{\mathrm{TFG}}(\mathrm{T_w}, \omega_t)$ at different temperatures, T=0K, 100K, 200K, and 300K. Upper and lower panels correspond to the cases of good time resolution (τ_f =12 fs) and good frequency resolution (τ_f= 60 fs), respectively. At T=0K, $S_{\mathrm{TFG}}(\mathrm{T_w}, \omega_t)$ (Fig. 1(a)) calculated with a short gate pulse (τ_f =12 fs) reflects the vibronic wave packet motions in the bright singlet $\mathrm{S_1}$ state. The spectrum exhibits periodic oscillations as a function of $\mathrm{T_w}$ modulated by the high frequency tuning mode Q_{t_1} with a period of ∼22 fs. One can also find the recurrence of the emission pattern with a longer period of ∼ 156 fs, which reveals the wave packet motions along tuning mode Q_{t_2} in the singlet $\mathrm{S_1}$ state. As waiting time $\mathrm{T_w}$ increases, the emission intensity slightly decreases due to the relatively slow population transfer from $\mathrm{S_1}$ to TT.

The spectrum $S_{\mathrm{TFG}}(\mathrm{T_w}, \omega_t)$ at T=100K, as displayed in Fig. 1(b), looks similar to that at T=0K. However, increasing temperature has two different effects on the spectrum. On the one hand, higher temperature leads to a faster S_1-TT population transfer, which is reflected by a slightly smaller intensity of the emission. On the other hand, it causes the dissipation of the vibrational energy to the bath, thus the spectral width of the emission at T=100K becomes narrower as compared to that at T=0K. With further increasing temperature to 200K and 300K (see Figs. 1(c) and (d)), the temperature effects become more pronounced as higher excited states of more vibrational modes are involved. As a result, the emission intensity further decreases with the temperature, indicating that high temperature facilitates the SF process. In addition, the spectral width of the emission narrows with the increase of temperature and vibrational structures on the left and right sides of the TFG spectra start to merge with increasing T_{w}, which can be attributed to the bath-induced dissipation of the vibrational energy.

The spectra $S_{\mathrm{TFG}}(\mathrm{T_w}, \omega_t)$ calculated with a longer gate pulse ($\tau_f = 60$ fs) at temperatures T=0K, 100K, 200K, and 300K are depicted in the lower panel of Fig. 1. As illustrated in Fig. 1(e), vibrational wave packet motions cannot be captured by the TFG spectrum with a longer gate pulse, the spectrum at T=0K consists of emissions from individual vibronic levels of the bright S_1 state. With the increase of the temperature, the individual emission lines are gradually merged, forming structureless, broaden signal (compare Figs. 1(f), (g) and (h) with Fig. 1(e)). The intensity of the emissions decreases with the temperature due to the faster S_1-TT population transfer at elevated temperatures.

The TA spectrum reflects the wave packet dynamics on both the electronic excited states (SE) and the electronic ground state (GSB), thus offering richer information content than that of the TFG fluorescence spectrum[76]. In Fig. 2, we display the dispersed transient absorption signal $S_{\mathrm{TA}}(\mathrm{T_w}, \omega_t)$ at different temperatures T=0K, 100K, 200K, and 300K. The TA spectrum at 0K (Fig. 2(a)) consists of a pronounced stationary ridge centred around 2.5 eV and periodic wave-like oscillations pattern with two characteristic periods of $\sim$ 22

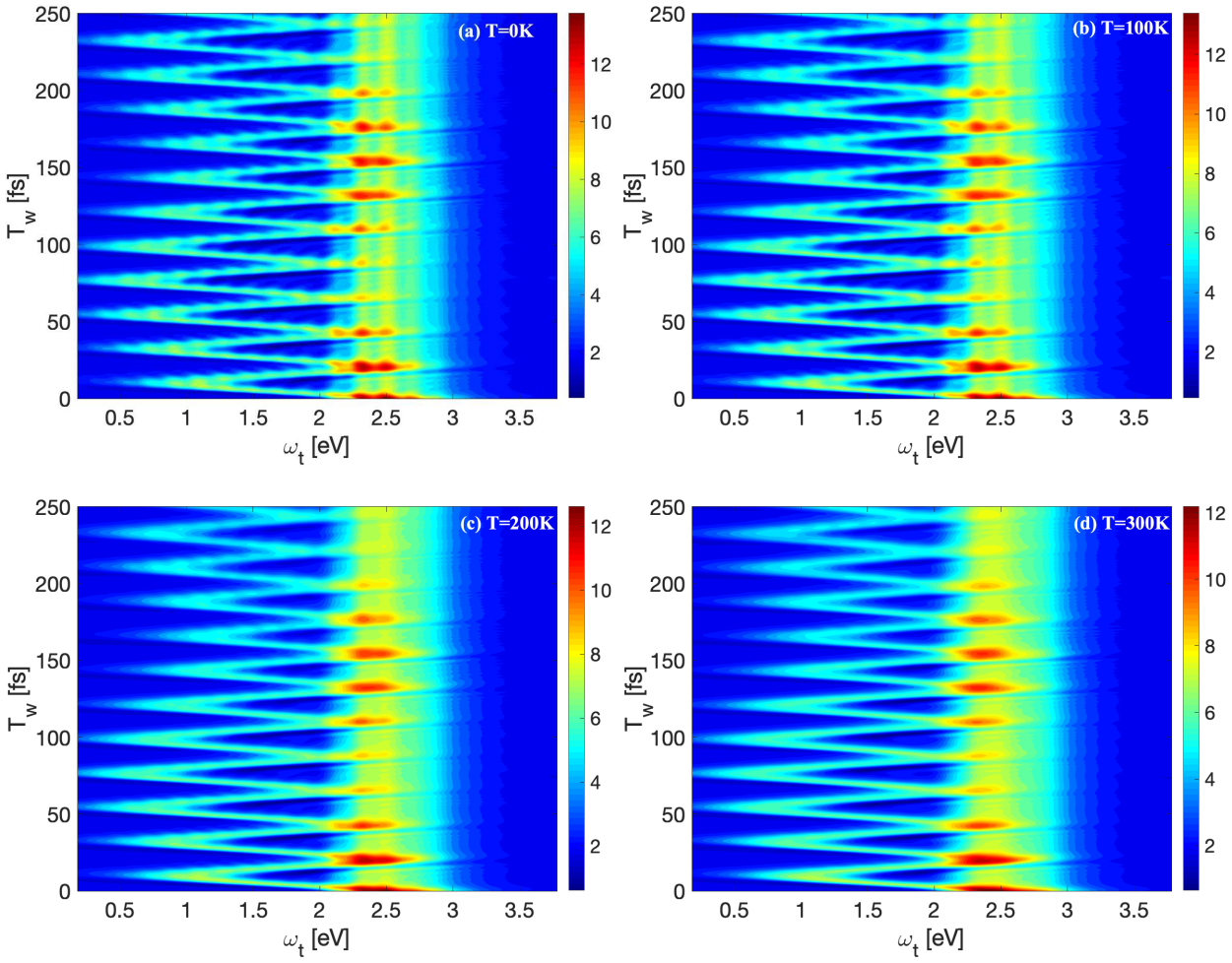

Figure 2: Dispersed transient absorption signal $S_{\mathrm{TA}}(\mathrm{T_w}, \omega_t)$ at different temperatures T=0K, 100K, 200K, and 300K.

and 156 fs. While the former originates in the GSB contribution, the latter results from the SE contribution. It should be noted that both the GSB and SE components contribute almost equally to the TA spectrum on the entire timescale of 250 fs. As shown in Figs. 2(b)-(d), the spectra are smoothed and broadened at elevated temperatures due to bath-induced dissipation of the vibrational energy. Furthermore, the intensity of the signal decreases with the rising temperature, which is attributed to a faster S_1-TT population transfer at higher temperatures.

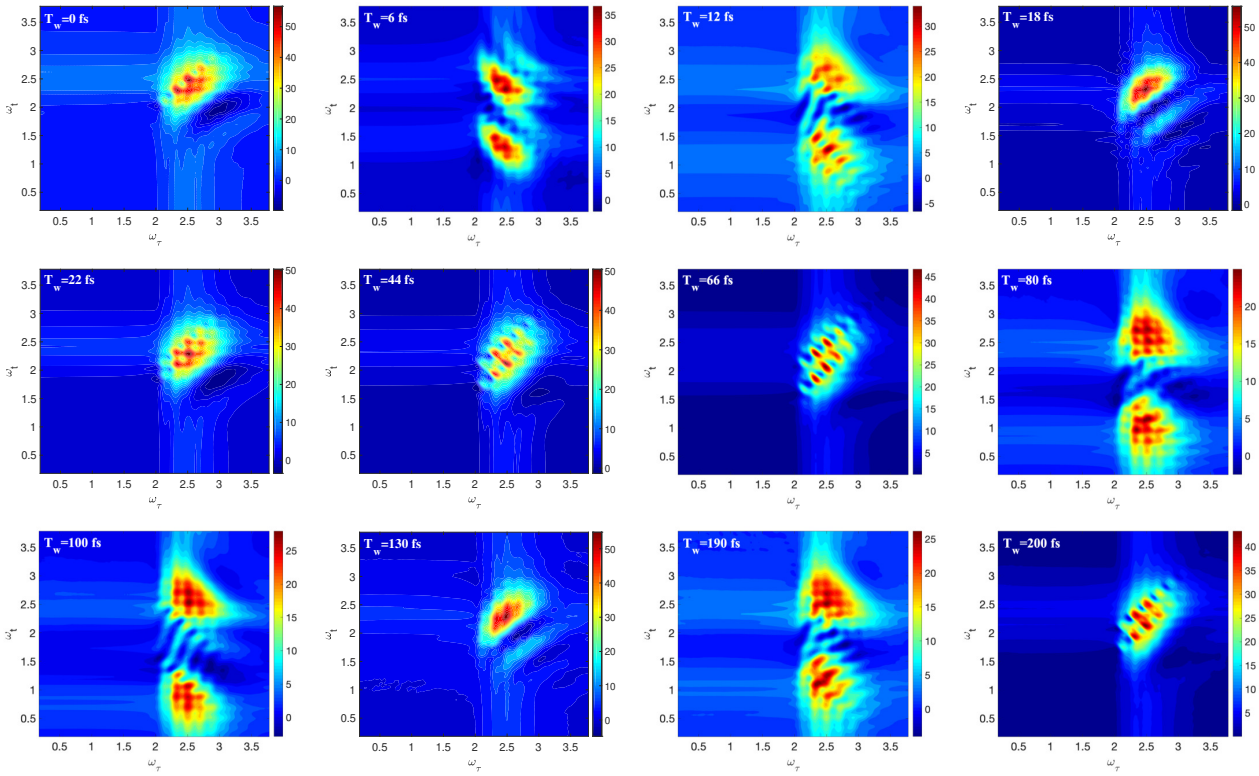

Figure 3: Real part of the total 2D electronic spectra $S(\omega_\tau, \mathrm{T_w}, \omega_t)$ at T=0K for different population times $\mathrm{T_w}$.

Electronic 2D spectroscopy captures the excitation and emission events on an equal footing, providing sensitive detection of wave packet motions on both electronic excited state (SE) and the electronic ground state (GSB). The 2D spectra $S(\omega_\tau, \mathrm{T_w}, \omega_t)$ as a function of population times $\mathrm{T_w}$ at four temperatures, T=0K, 100K, 200K, and 300K, are displayed in Figs. 3-6. Let us consider the time evolution of the 2D spectra at T=0K as shown in Fig. 3 first. The 2D spectra at $\mathrm{T_w}$=0 fs exhibit a pronounced vibrationally diagonal multi-peak

structure with an energy spacing of $\sim \Omega_{t_1}$, which corresponds to the vibrational progression of the linear absorption. The shape of the 2D spectrum is dominated by a superposition of the spectrally overlapping SE and GSB contributions. At T_w=6 fs, the SE peaks move along the ω_t axis to lower energies, reflecting the wave packet movement along the excited state PES to the lower energy region. The spectral shape of the GSB contribution also changes, while its "center of gravity" remains around the initial position $\omega_t = \omega_\tau \approx 2.5$ eV. As T_w increases to 12 fs, the SE peaks reach for the first time the attainable lowest energy region (see Figs. 1(a) and 2(a)). From T_w=12 fs to T_w=22 fs, the SE peaks then move up along the ω_t axis due to the reverse movement of the wave packet along the excited state PES. When the wave packet returns back to its starting points on the excited state PES at T_w=22 fs, the GSB and SE contributions overlap again and one can observe almost complete revival of the 2D spectra as compared to the spectra at T_w=0 fs. With the further increase of T_w, the 2D spectra show periodic oscillation which is predominately modulated as a function of T_w by the high-frequency tuning mode Q_{t_1} with a vibrational period of $\sim$ 22 fs (compare spectra at T_w=44, 66, and 200 fs, as well as the spectra at T_w=18 and 130 fs). In addition, the recurrence of the spectra at T_w=200 fs as compared to those at T_w=44 fs also reveals the wave packet motions along the low-frequency tuning mode Q_{t_2} with a vibrational period of $\sim$ 159 fs. It should be noted that 2D spectra at three representative population times T_w=80, 100, and 190 fs show a large energy separation between the GSB and SE peaks along the ω_t axis, a feature that is consistent with accessible lowest frequency region in the time-resolved fluorescence and TA spectra (see Figs. 1(a) and 2(a)). Overall, the time evolution of 2D spectra vividly maps the wave packet dynamics on both electronic excited state and the electronic ground state.

The 2D spectra at T=100K for different population times T_w are depicted in Fig. 4. While these spectra show quite similar vibrational peaks structure and periodic oscillations as a function of T_w as compared to their counterparts at zero temperature in Fig. 3, the differences between the two groups of signals can be discernible. The rising temperature

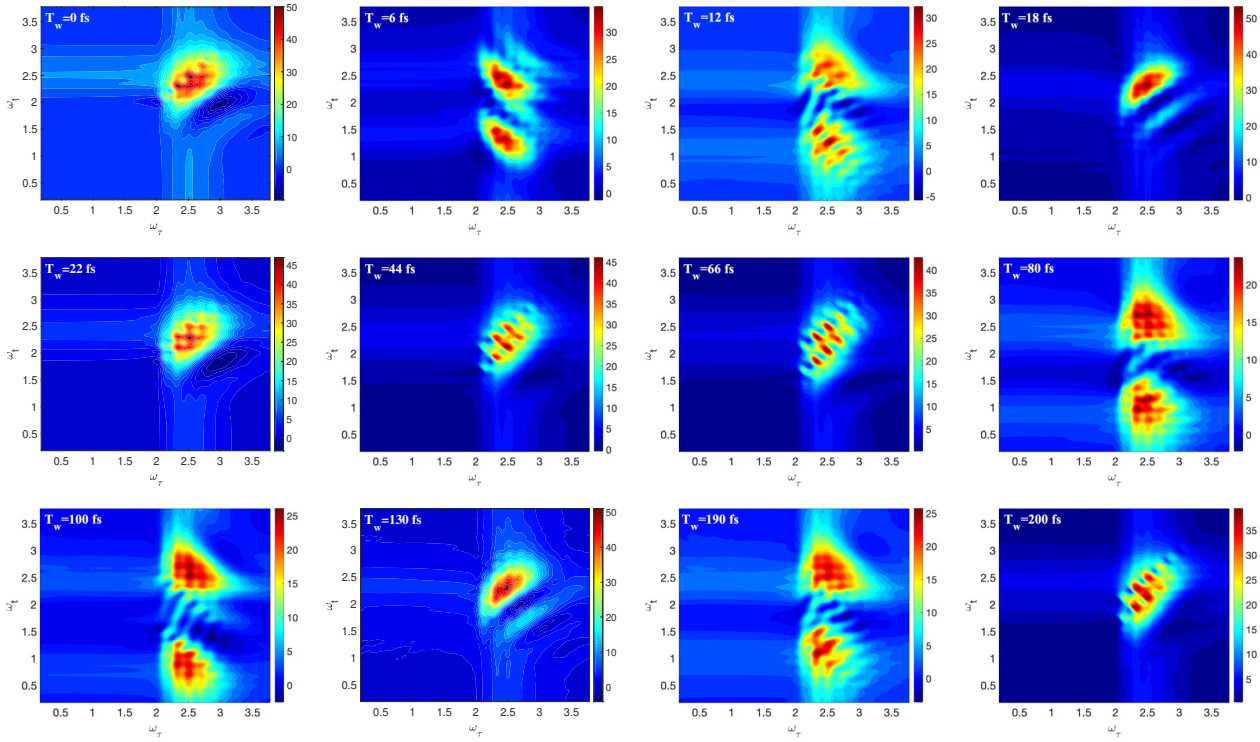

Figure 4: Real part of the total 2D electronic spectra $S(\omega_\tau, \mathrm{T_w}, \omega_t)$ at T=100K for different population times $\mathrm{T_w}$.

primarily affects the 2D spectra in two ways. Firstly, it increases the number of the vibronic states which can be probed by the laser pulse. As a result, the overall peak intensities of 2D spectra for each specific $\mathrm{T_w}$ are slightly decreased as temperature increases to 100K, which can be attributed to a faster $\mathrm{S_1}$-TT population transfer at T=100K. Secondly, higher temperature induces stronger dissipation of the vibrational energy to the bath, which in turn leads to broadened vibrational peaks. When the temperature further increases to T=200K (Fig. 5) and T=300K (Fig. 6), the above two effects of temperature on spectra become more pronounced. It is found that the overall intensities of 2D spectra for each specific $\mathrm{T_w}$ further decrease with temperature due to the faster SF process at elevated temperatures. Furthermore, the individual vibrational subpeaks are blurred out and merged into broad features at high temperatures, a direct consequence of the strong bath-induced electronic dephasing.

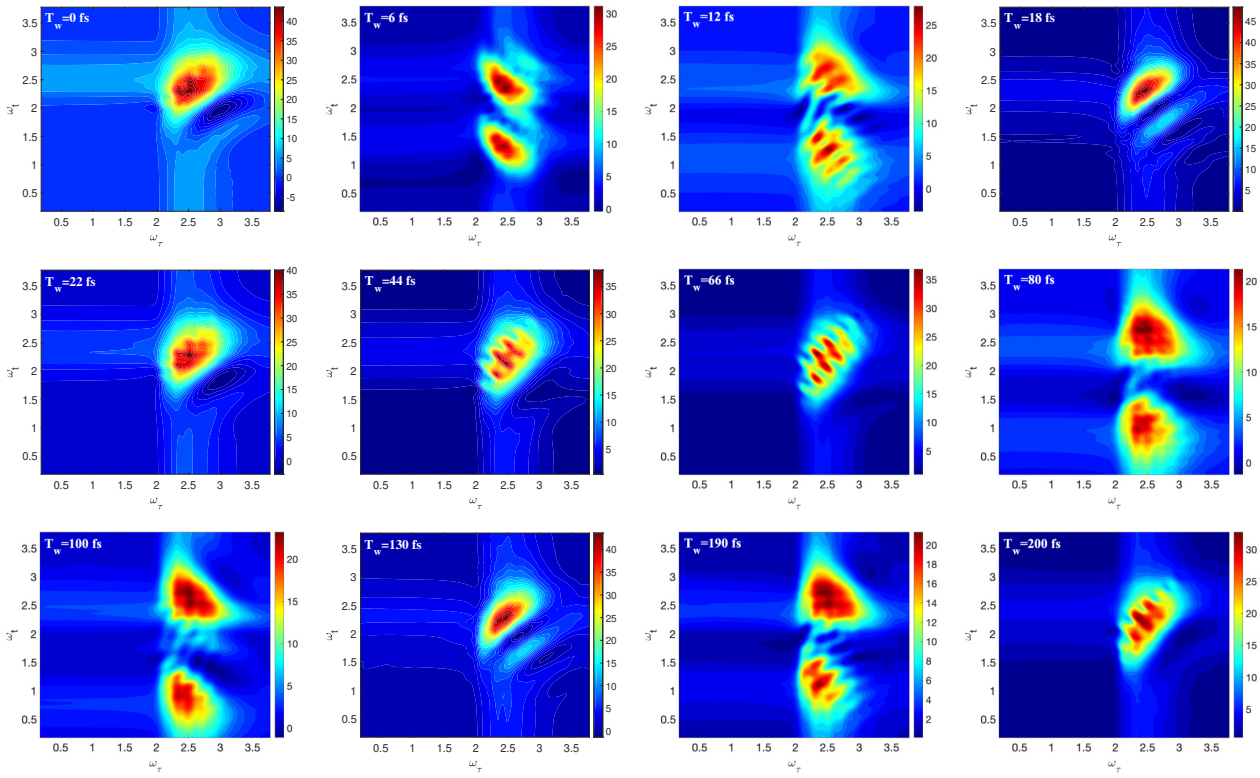

Figure 5: Real part of the total 2D electronic spectra $S(\omega_\tau, \mathrm{T_w}, \omega_t)$ at T=200K for different population times $\mathrm{T_w}$.

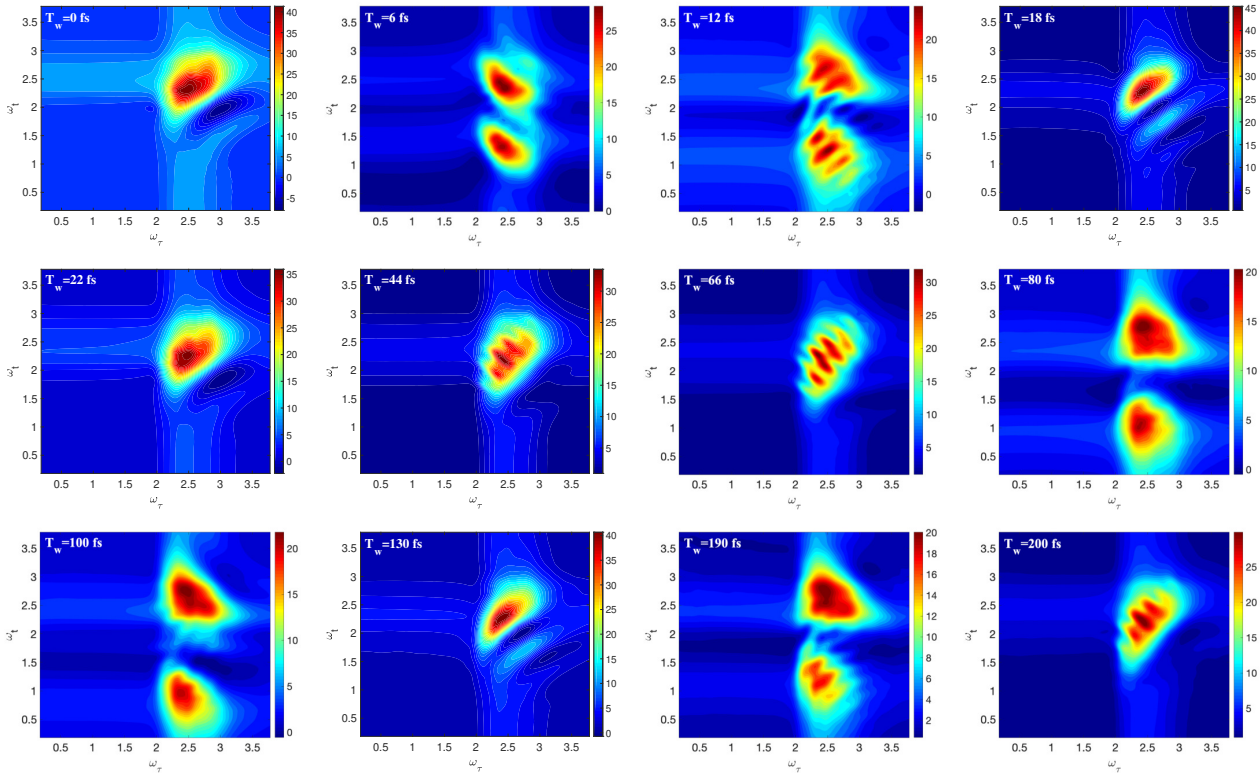

Figure 6: Real part of the total 2D electronic spectra $S(\omega_\tau, \mathrm{T_w}, \omega_t)$ at T=300K for different population times $\mathrm{T_w}$.

4 Conclusions

In summary, we have developed a new approach to the computation of time and frequency-resolved 4WM signals at finite temperatures by integrating the MCE method into the framework of the TFD theory. The proposed method employs the formalism of the TFD to transform the four-time correlation function at finite temperatures into a form which can be treated as the four-time correlation function at zero temperature with an augmented vibrational Hilbert space twice as large.

The strengths of the theory developed in this work have been demonstrated by simulating three typical multidimensional spectroscopic signals, namely, the time and frequency-resolved fluorescence spectra, the transient-absorption pump-probe spectra, and the electronic 2D spectra at finite temperatures, for a CI-mediated SF model of crystalline rubrene. While the time and frequency-resolved fluorescence spectrum reflects the vibrational wave-packet motions on the electronic excited state, the transient absorption and electronic 2D spectra provide sensitive detection of the vibrational wave packet dynamics on both electronic excited state (SE) and the electronic ground state (GSB). The rising temperature has two main effects on the spectra. On the one hand, increasing temperature causes lower intensities of the TFG fluorescence, TA and 2D electronic spectra, which can be ascribed to the faster SF process at elevated temperature. On the other hand, higher temperature induces stronger dissipation of vibrational energy to the bath, which in turn leads to a narrower spectral width of the TFG fluorescence spectra and broaden peaks of TA and 2D spectra.

Finally, a short outlook on possible extensions of our approach and its applications. To properly describe the excited state absorption (ESA) contribution to the TA and 2D measurements of various SF process[65,77], one also needs to consider higher-lying singlet/triplet states. Our theory can take into account the ESA by propagating the system in the higher excited state manifold between τ_2 and τ_3 in Eq. 21, with $\hat{\tilde{h}}_{g\theta}$ substituted by $\hat{\tilde{H}}_{f\theta} = e^{i\hat{G}}\left(\hat{H}_f - \hat{\tilde{h}}_g\right)e^{-i\hat{G}}$ ($\hat{H}_f$ represents the Hamiltonian for higher-lying electronic excited states). It should be noted

that the MCE method (MCEv1) used in this work was developed for the simulations of model systems, which require a tedious construction of global or semi-global PESs. The independent-trajectory version of the MCE method (MCEv2, see Appendix B), in contrast, avoids the calculation of PESs and is well suited to the on-the-fly *ab initio* (OTF-AI) simulations of non-adiabatic excited state molecular dynamics of small polyatomic molecules[42,78,79]. It is thus of great interest to extend our approach to the OTF-AI evaluation of various 4WM signals of small polyatomic molecules at finite temperatures by combining the MCEv2 method with the TFD theory. Work in these directions is in progress.

Acknowledgement

The authors would like to thank Kewei Sun for useful discussions. L. P. C acknowledges support from the Max-Planck Gesellschaft via the MPI-PKS visitors program. D. V. S. acknowledges EPSRC (Grant No. EP/P021123/1). Y. Z would like to thank the support of the Singapore Ministry of Education Academic Research Fund Tier 1 (Grant Nos. 2018-T1-002-175 and 2020-T1-002-075). M. F. G acknowledges support of Hangzhou Dianzi University through the startup funding. This work was undertaken on ARC3, part of the High Performance Computing facilities at the University of Leeds, UK.

Appendix A Derivation of Eq. 17

The proof of Eq. 17 proceeds as follows

$$
\begin{aligned}
& \Phi(\tau_4,\tau_3,\tau_2,\tau_1) \\
= \;& \mathrm{Tr}\left(\hat{\rho}_g\langle g|e^{i\hat{h}_g\tau_4}\boldsymbol{\mu}_- e^{-i\hat{H}_e(\tau_4-\tau_3)}\boldsymbol{\mu}_+ e^{-i\hat{h}_g(\tau_3-\tau_2)}\boldsymbol{\mu}_- e^{-i\hat{H}_e(\tau_2-\tau_1)}\boldsymbol{\mu}_+ e^{-i\hat{h}_g\tau_1}|g\rangle\right) \\
= \;& \mathrm{Tr}\left(\langle g|\hat{\rho}_g^{1/2}\boldsymbol{\mu}_- e^{-i\hat{H}_e(\tau_4-\tau_3)}\boldsymbol{\mu}_+ e^{-i\hat{h}_g(\tau_3-\tau_2)}\boldsymbol{\mu}_- e^{-i\hat{H}_e(\tau_2-\tau_1)}\boldsymbol{\mu}_+\hat{\rho}_g^{1/2}e^{i\hat{h}_g\tau_4}e^{-i\hat{h}_g\tau_1}|g\rangle\right) \\
= \;& \langle g|\sum_l\langle l|\hat{\rho}_g^{1/2}\boldsymbol{\mu}_- e^{-i\hat{H}_e(\tau_4-\tau_3)}\boldsymbol{\mu}_+ e^{-i\hat{h}_g(\tau_3-\tau_2)}\boldsymbol{\mu}_- e^{-i\hat{H}_e(\tau_2-\tau_1)}\boldsymbol{\mu}_+\hat{\rho}_g^{1/2}e^{i\hat{h}_g\tau_4}e^{-i\hat{h}_g\tau_1}|l\rangle|g\rangle \\
= \;& \langle g|\sum_l\sum_{l'}\langle l|\hat{\rho}_g^{1/2}\boldsymbol{\mu}_- e^{-i\hat{H}_e(\tau_4-\tau_3)}\boldsymbol{\mu}_+ e^{-i\hat{h}_g(\tau_3-\tau_2)}\boldsymbol{\mu}_- e^{-i\hat{H}_e(\tau_2-\tau_1)}\boldsymbol{\mu}_+\hat{\rho}_g^{1/2}|l'\rangle\langle l'|e^{i\hat{h}_g\tau_4}e^{-i\hat{h}_g\tau_1}|l\rangle|g\rangle \\
= \;& \langle g|\sum_l\sum_{l'}\langle l|\hat{\rho}_g^{1/2}\boldsymbol{\mu}_- e^{-i\hat{H}_e(\tau_4-\tau_3)}\boldsymbol{\mu}_+ e^{-i\hat{h}_g(\tau_3-\tau_2)}\boldsymbol{\mu}_- e^{-i\hat{H}_e(\tau_2-\tau_1)}\boldsymbol{\mu}_+\hat{\rho}_g^{1/2}|l'\rangle\langle\tilde{l}|e^{i\hat{\tilde{h}}_g\tau_4}e^{-i\hat{\tilde{h}}_g\tau_1}|\tilde{l'}\rangle|g\rangle \\
= \;& \langle g|\sum_l\langle l|\langle\tilde{l}|\hat{\rho}_g^{1/2}e^{i\hat{\tilde{h}}_g\tau_4}\boldsymbol{\mu}_- e^{-i\hat{H}_e(\tau_4-\tau_3)}\boldsymbol{\mu}_+ e^{-i\hat{h}_g(\tau_3-\tau_2)}\boldsymbol{\mu}_- e^{-i\hat{H}_e(\tau_2-\tau_1)}\boldsymbol{\mu}_+ e^{-i\hat{\tilde{h}}_g\tau_1}\hat{\rho}_g^{1/2}\sum_{l'}|l'\rangle|\tilde{l'}\rangle|g\rangle \\
= \;& \langle g|\langle\mathbf{0}(\beta)|\boldsymbol{\mu}_- e^{-i(\hat{H}_e-\hat{\tilde{h}}_g)(\tau_4-\tau_3)}\boldsymbol{\mu}_+ e^{-i(\hat{h}_g-\hat{\tilde{h}}_g)(\tau_3-\tau_2)}\boldsymbol{\mu}_- e^{-i(\hat{H}_e-\hat{\tilde{h}}_g)(\tau_2-\tau_1)}\boldsymbol{\mu}_+|\mathbf{0}(\beta)\rangle|g\rangle \qquad \text{(A1)}
\end{aligned}
$$

where we have used the identity $\langle l'|e^{i\hat{h}_g\tau_4}e^{-i\hat{h}_g\tau_1}|l\rangle = \langle\tilde{l}|e^{i\hat{\tilde{h}}_g\tau_4}e^{-i\hat{\tilde{h}}_g\tau_1}|\tilde{l'}\rangle$

Appendix B The multiconfigurational Ehrenfest method

Upon laser excitation the system is excited from the electronic ground state to the electronic excited states, and the resulting dynamics can be described by the TDSE. The MCE method, in which the wave function is expanded as a linear combination of many configurations with each configuration guided by its own Ehrenfest (mean-field) trajectory, has been proved as a numerical efficient and accurate tool for simulating quantum dynamics involving multiple electronic states. There are two versions of the MCE method (MCEv1 and MCEv2). In the MCEv1 method, the wave function is represented as a linear combination

of M configurations[41]

$$
\begin{aligned}
|\Psi(t)\rangle = & \sum_{u=1}^{M}\left(\sum_{e}^{\mathrm{N_e}} A_{ue}(t)|e\rangle\right)|\mathbf{z}_u(t)\rangle \\
= & \sum_{u=1}^{M}\left(\sum_{e}^{\mathrm{N_e}} A_{ue}(t)|e\rangle\right)\exp\left[\sum_{l}^{\mathrm{N_{mod}}}\left(z_{ul}(t)\hat{b}_l^{\dagger}-z_{ul}^{*}(t)\hat{b}_l\right)\right]|0\rangle_g
\end{aligned}
\tag{B1}
$$

Here, u is the index for the configuration. A_{ue} is the amplitude in the diabatic electronic excited state $|e\rangle$, and $|\mathbf{z}_u\rangle$ is the coherent state for the vibrational DOFs. z_{ul} is the phonon displacement for the lth normal mode and $|0\rangle_g$ is the vibrational ground state of $\hat{h}_g$. The MCEv1 method was shown to provide a reliable description of the dynamics of multi-state multi-mode model systems, such as spin-boson model[41] and one-dimensional Holstein polaron model[43]. The MCEv2 method, on the other hand, was developed for the use with on-the-fly *ab initio* simulations of ultrafast nonadiabatic excited-state processes of small polyatomic molecules[78,79]. Compared to the MCEv1 method in which the Ehrenfest trajectories are coupled with each other, in the MCEv2 method, the wave function is expanded using an ensemble of independent Ehrenfest configurations[42]

$$
\begin{aligned}
|\Psi(t)\rangle = & \sum_{u=1}^{M} D_u(t)|\phi_u(t)\rangle \\
= & \sum_{u=1}^{M} D_u(t)\left(\sum_{e}^{\mathrm{N_e}} A_{ue}(t)|e\rangle\right)|\mathbf{z}_u(t)\rangle
\end{aligned}
\tag{B2}
$$

Here, D_u are weighting coefficients for the configurations $|\phi_u(t)\rangle = \left(\sum_e^{\mathrm{N_e}} A_{ue}(t)|e\rangle\right)|\mathbf{z}_u(t)\rangle$. Since the Ehrenfest trajectories now are independent with each other, the MCEv2 method is well suited to be implemented with an on-the-fly *ab initio* calculation of the electronic structure, but is also harder to converge for some systems.

In this work, we use the MCEv1 method to solve the TDSE due to its faster convergence as compared to that of the MCEv2 method. The equations of motion for the state amplitudes

A_{ue} can be derived by first constructing the following Lagrangian,

$$\begin{aligned} L = \quad & \langle\Psi(t)|\frac{i}{2}\frac{\overleftrightarrow{\partial}}{\partial t} - \hat{H}_e|\Psi(t)\rangle \\ = \quad & \frac{i}{2}\sum_{nu}^{M}\sum_{e}^{\mathrm{N_e}}\left\{\left[A^*_{ne}\dot{A}_{ue} - \dot{A}^*_{ne}A_{ue}\right] + A^*_{ne}A_{ue}\sum_l\left(\frac{z_{nl}\dot{z}^*_{nl} + \dot{z}_{nl}z^*_{nl} - z_{ul}\dot{z}^*_{ul} - \dot{z}_{ul}z^*_{ul}}{2} + z^*_{nl}\dot{z}_{ul} - \dot{z}^*_{nl}z_{ul}\right)\right\} \\ & \times R_{nu} - \langle\Psi(t)|\hat{H}_e|\Psi(t)\rangle \end{aligned} \tag{B3}$$

where

$$R_{nu} = \langle\mathbf{z}_n|\mathbf{z}_u\rangle = \exp\left\{\sum_l z^*_{nl}z_{ul} - \frac{1}{2}\left(|z_{nl}|^2 + |z_{ul}|^2\right)\right\} \tag{B4}$$

and

$$\langle\Psi(t)|\hat{H}_e|\Psi(t)\rangle = \sum_{nu}^{M}\left(\sum_{ee'}^{\mathrm{N_e}} A^*_{ne}A_{ue'}h^{\mathrm{ord}}_{ee'}(\mathbf{z}^*_n,\mathbf{z}_u)\right)R_{nu} \tag{B5}$$

then the application of the Euler equations

$$\frac{\partial L}{\partial A^*_{ne}} - \frac{d}{dt}\frac{\partial L}{\partial \dot{A}^*_{ne}} = 0 \tag{B6}$$

yields

$$i\sum_{u}^{M}\left\{\dot{A}_{ue} + A_{ue}\sum_l\left[z^*_{nl}\dot{z}_{ul} - \frac{\dot{z}_{ul}z^*_{ul} + z_{ul}\dot{z}^*_{ul}}{2}\right]\right\}R_{nu} - \sum_{u}^{M}\sum_{e'}^{\mathrm{N_e}} A_{ue'}h^{\mathrm{ord}}_{ee'}(\mathbf{z}^*_n,\mathbf{z}_u)R_{nu} = 0 \tag{B7}$$

In the MCEv1 method, the equations of motion for $\mathbf{z}_u$ are obtained by applying the Ehrenfest

dynamics to each $\mathbf{z}_u$, i.e.,

$$\begin{aligned} i\dot{\mathbf{z}}_u = & \quad \frac{\partial H_u^{\mathrm{Ehr}}}{\partial \mathbf{z}_u^*}, \\ H_u^{\mathrm{Ehr}} = & \quad \frac{\langle \Psi_u | \hat{H}_e | \Psi_u \rangle}{\langle \Psi_u | \Psi_u \rangle}, \\ |\Psi_u\rangle = & \quad \sum_e^{\mathrm{N_e}} A_{ue} |e\rangle |\mathbf{z}_u\rangle. \end{aligned} \tag{B8}$$

with

$$\langle \Psi_u | \hat{H}_e | \Psi_u \rangle = \quad \sum_{ee'}^{\mathrm{N_e}} A_{ue}^* A_{ue'} h_{ee'}^{\mathrm{ord}}(\mathbf{z}_u^*, \mathbf{z}_u), \tag{B9}$$

$$\langle \Psi_u | \Psi_u \rangle = \quad \sum_{e}^{\mathrm{N_e}} A_{ue}^* A_{ue} \tag{B10}$$

For the singlet fission model described in Sec. 2.3, the equations of motion for the state amplitude A_{ue} and phonon displacement z_{ul} can be derived as

$$\begin{aligned} & i\sum_u^M \left\{ \dot{A}_{u\mathrm{S}_1} + A_{u\mathrm{S}_1} \sum_l \left[z_{nl}^* \dot{z}_{ul} - \frac{\dot{z}_{ul} z_{ul}^* + z_{ul} \dot{z}_{ul}^*}{2} \right] \right\} R_{nu} \\ = & \quad \sum_u^M \left\{ A_{u\mathrm{S}_1} \left[\epsilon_{\mathrm{S}_1} + \sum_l \omega_l^{'} z_{nl}^* z_{ul} + \sum_l \frac{\kappa_l^{'(\mathrm{S}_1)}}{\sqrt{2}} (z_{nl}^* + z_{ul}) \right] + A_{u\mathrm{TT}} \sum_l \frac{\lambda_l^{'}}{\sqrt{2}} (z_{nl}^* + z_{ul}) \right\} R_{nu} \\ & i\sum_u^M \left\{ \dot{A}_{u\mathrm{TT}} + A_{u\mathrm{TT}} \sum_l \left[z_{nl}^* \dot{z}_{ul} - \frac{\dot{z}_{ul} z_{ul}^* + z_{ul} \dot{z}_{ul}^*}{2} \right] \right\} R_{nu} \\ = & \quad \sum_u^M \left\{ A_{u\mathrm{TT}} \left[\epsilon_{\mathrm{TT}} + \sum_l \omega_l^{'} z_{nl}^* z_{ul} + \sum_l \frac{\kappa_l^{'(\mathrm{TT})}}{\sqrt{2}} (z_{nl}^* + z_{ul}) \right] + A_{u\mathrm{S}_1} \sum_l \frac{\lambda_l^{'}}{\sqrt{2}} (z_{nl}^* + z_{ul}) \right\} R_{nu} \end{aligned} \tag{B11}$$

$$i\dot{z}_{ul} = \frac{A_{u\mathrm{S}_1}^* A_{u\mathrm{S}_1} (\omega_l^{'} z_{ul} + \frac{\kappa_l^{'(\mathrm{S}_1)}}{\sqrt{2}}) + A_{u\mathrm{TT}}^* A_{u\mathrm{TT}} (\omega_l^{'} z_{ul} + \frac{\kappa_l^{'(\mathrm{TT})}}{\sqrt{2}}) + (A_{u\mathrm{S}_1}^* A_{u\mathrm{TT}} + A_{u\mathrm{TT}}^* A_{u\mathrm{S}_1}) \frac{\lambda_l^{'}}{\sqrt{2}}}{A_{u\mathrm{S}_1}^* A_{u\mathrm{S}_1} + A_{u\mathrm{TT}}^* A_{u\mathrm{TT}}} \tag{B12}$$

By inserting the wave function of the MCEv1 method (Eq. B1) into Eq. 13, we obtain

the expressions of the four response functions R_a [64], $a = 1, 2, 3, 4$, at zero temperature.

$$
\begin{aligned}
R_1(\tau, T_{\rm w}, t) = \quad & \sum_{nu}^{\rm M} \sum_{e_1,e_2,e_3,e_4} \left(\mathbf{s}_4^* \cdot \boldsymbol{\mu}_{ge_3}\right) \left(\mathbf{s}_1 \cdot \boldsymbol{\mu}_{e_4 g}\right) \left(\mathbf{s}_2^* \cdot \boldsymbol{\mu}_{ge_1}\right) \left(\mathbf{s}_3 \cdot \boldsymbol{\mu}_{e_2 g}\right) A_{ne_2}^{e_1 *}(T_{\rm w}) A_{ue_3}^{e_4}(\tau + T_{\rm w} + t) \\
& \times \exp\left\{ \sum_l z_{nl}^{e_1 *}(T_{\rm w}) z_{ul}^{e_4}(\tau + T_{\rm w} + t) e^{i\omega_l t} \right\} e^{-\frac{1}{2}\sum_l \left(|z_{nl}^{e_1}(T_{\rm w})|^2 + |z_{ul}^{e_4}(\tau + T_{\rm w} + t)|^2\right)}, \\
R_2(\tau, T_{\rm w}, t) = \quad & \sum_{nu}^{\rm M} \sum_{e_1,e_2,e_3,e_4} \left(\mathbf{s}_4^* \cdot \boldsymbol{\mu}_{ge_3}\right) \left(\mathbf{s}_1^* \cdot \boldsymbol{\mu}_{ge_1}\right) \left(\mathbf{s}_2 \cdot \boldsymbol{\mu}_{e_4 g}\right) \left(\mathbf{s}_3 \cdot \boldsymbol{\mu}_{e_2 g}\right) A_{ne_2}^{e_1 *}(\tau + T_{\rm w}) A_{ue_3}^{e_4}(t + T_{\rm w}) \\
& \times \exp\left\{ \sum_l z_{nl}^{e_1 *}(\tau + T_{\rm w}) z_{ul}^{e_4}(t + T_{\rm w}) e^{i\omega_l t} \right\} e^{-\frac{1}{2}\sum_l \left(|z_{nl}^{e_1}(\tau + T_{\rm w})|^2 + |z_{ul}^{e_4}(t + T_{\rm w})|^2\right)}, \\
R_3(\tau, T_{\rm w}, t) = \quad & \sum_{nu}^{\rm M} \sum_{e_1,e_2,e_3,e_4} \left(\mathbf{s}_4^* \cdot \boldsymbol{\mu}_{ge_3}\right) \left(\mathbf{s}_1^* \cdot \boldsymbol{\mu}_{ge_1}\right) \left(\mathbf{s}_2 \cdot \boldsymbol{\mu}_{e_2 g}\right) \left(\mathbf{s}_3 \cdot \boldsymbol{\mu}_{e_4 g}\right) A_{ne_2}^{e_1 *}(\tau) A_{ue_3}^{e_4}(t) \\
& \times \exp\left\{ \sum_l z_{nl}^{e_1 *}(\tau) z_{ul}^{e_4}(t) e^{i\omega_l (T_{\rm w} + t)} \right\} e^{-\frac{1}{2}\sum_l \left(|z_{nl}^{e_1}(\tau)|^2 + |z_{ul}^{e_4}(t)|^2\right)}, \\
R_4(\tau, T_{\rm w}, t) = \quad & \sum_{nu}^{\rm M} \sum_{e_1,e_2,e_3,e_4} \left(\mathbf{s}_4^* \cdot \boldsymbol{\mu}_{ge_1}\right) \left(\mathbf{s}_1 \cdot \boldsymbol{\mu}_{e_4 g}\right) \left(\mathbf{s}_2^* \cdot \boldsymbol{\mu}_{ge_3}\right) \left(\mathbf{s}_3 \cdot \boldsymbol{\mu}_{e_2 g}\right) A_{ne_2}^{e_1 *}(-t) A_{ue_3}^{e_4}(\tau), \\
& \times \exp\left\{ \sum_l z_{nl}^{e_1 *}(-t) z_{ul}^{e_4}(\tau) e^{-i\omega_l T_{\rm w}} \right\} e^{-\frac{1}{2}\sum_l \left(|z_{nl}^{e_1}(-t)|^2 + |z_{ul}^{e_4}(\tau)|^2\right)}, \qquad \text{(B13)}
\end{aligned}
$$

where $\mathbf{s}_4$ is the polarization of the local oscillator field, $A_{ue_3}^{e_4}(t)$ is the probability to find the electronic state e_3 at time t if we excite the system from the electronic ground state to the electronic excited state e_4 initially and with configuration u, and $z_{ul}^{e_4}(t)$ is the corresponding phonon displacement at time t.

The expressions for the four response functions R_a, $a = 1, 2, 3, 4$, at finite temperatures can be obtained in a same way as the zero temperature case by inserting the wave function

of Eq. 35 into Eq. 24. We have

$$
\begin{aligned}
R_1(\tau,T_{\rm w},t) = \quad & \sum_{nu}^{\rm M}\sum_{e_1,e_2,e_3,e_4} \left(\mathbf{s}_4^*\cdot\boldsymbol{\mu}_{ge_3}\right)\left(\mathbf{s}_1\cdot\boldsymbol{\mu}_{e_4g}\right)\left(\mathbf{s}_2^*\cdot\boldsymbol{\mu}_{ge_1}\right)\left(\mathbf{s}_3\cdot\boldsymbol{\mu}_{e_2g}\right) A^{e_1*}_{ne_2}(T_{\rm w})A^{e_4}_{ue_3}\left(\tau+T_{\rm w}+t\right) \\
& \times\exp\left\{\sum_{l}^{2{\rm N}_{\rm mod}} z^{e_1*}_{nl}(T_{\rm w})z^{e_4}_{ul}(\tau+T_{\rm w}+t)e^{i\omega_l' t}\right\} e^{-\frac{1}{2}\sum_l^{2{\rm N}_{\rm mod}}\left(|z^{e_1}_{nl}(T_{\rm w})|^2+|z^{e_4}_{ul}(\tau+T_{\rm w}+t)|^2\right)} \\
R_2(\tau,T_{\rm w},t) = \quad & \sum_{nu}^{\rm M}\sum_{e_1,e_2,e_3,e_4} \left(\mathbf{s}_4^*\cdot\boldsymbol{\mu}_{ge_3}\right)\left(\mathbf{s}_1^*\cdot\boldsymbol{\mu}_{ge_1}\right)\left(\mathbf{s}_2\cdot\boldsymbol{\mu}_{e_4g}\right)\left(\mathbf{s}_3\cdot\boldsymbol{\mu}_{e_2g}\right) A^{e_1*}_{ne_2}(\tau+T_{\rm w})A^{e_4}_{ue_3}(t+T_{\rm w}) \\
& \times\exp\left\{\sum_{l}^{2{\rm N}_{\rm mod}} z^{e_1*}_{nl}(\tau+T_{\rm w})z^{e_4}_{ul}(t+T_{\rm w})e^{i\omega_l' t}\right\} e^{-\frac{1}{2}\sum_l^{2{\rm N}_{\rm mod}}\left(|z^{e_1}_{nl}(\tau+T_{\rm w})|^2+|z^{e_4}_{ul}(t+T_{\rm w})|^2\right)} \\
R_3(\tau,T_{\rm w},t) = \quad & \sum_{nu}^{\rm M}\sum_{e_1,e_2,e_3,e_4} \left(\mathbf{s}_4^*\cdot\boldsymbol{\mu}_{ge_3}\right)\left(\mathbf{s}_1^*\cdot\boldsymbol{\mu}_{ge_1}\right)\left(\mathbf{s}_2\cdot\boldsymbol{\mu}_{e_2g}\right)\left(\mathbf{s}_3\cdot\boldsymbol{\mu}_{e_4g}\right) A^{e_1*}_{ne_2}(\tau)A^{e_4}_{ue_3}(t) \\
& \times\exp\left\{\sum_{l}^{2{\rm N}_{\rm mod}} z^{e_1*}_{nl}(\tau)z^{e_4}_{ul}(t)e^{i\omega_l'(T_{\rm w}+t)}\right\} e^{-\frac{1}{2}\sum_l^{2{\rm N}_{\rm mod}}\left(|z^{e_1}_{nl}(\tau)|^2+|z^{e_4}_{ul}(t)|^2\right)} \\
R_4(\tau,T_{\rm w},t) = \quad & \sum_{nu}^{\rm M}\sum_{e_1,e_2,e_3,e_4} \left(\mathbf{s}_4^*\cdot\boldsymbol{\mu}_{ge_1}\right)\left(\mathbf{s}_1\cdot\boldsymbol{\mu}_{e_4g}\right)\left(\mathbf{s}_2^*\cdot\boldsymbol{\mu}_{ge_3}\right)\left(\mathbf{s}_3\cdot\boldsymbol{\mu}_{e_2g}\right) A^{e_1*}_{ne_2}(-t)A^{e_4}_{ue_3}(\tau) \\
& \times\exp\left\{\sum_{l}^{2{\rm N}_{\rm mod}} z^{e_1*}_{nl}(-t)z^{e_4}_{ul}(\tau)e^{-i\omega_l' T_{\rm w}}\right\} e^{-\frac{1}{2}\sum_l^{2{\rm N}_{\rm mod}}\left(|z^{e_1}_{nl}(-t)|^2+|z^{e_4}_{ul}(\tau)|^2\right)} \qquad \text{(B14)}
\end{aligned}
$$

References

(1) Abramavicius, D.; Palmieri, B.; Voronine, D. V.; Šanda, F.; Mukamel, S. Coherent Multidimensional Optical Spectroscopy of Excitons in Molecular Aggregates; Quasiparticle versus Supermolecule Perspectives. *Chem. Rev.* **2009**, *109*, 2350-2408.

(2) Clarke, T. M.; Durrant, J. R. Charge photogeneration in organic solar cells. *Chem. Rev.* **2010**, *110*, 6736-6767.

(3) Chen, L. P.; Shenai, P.; Zheng, F. L.; Somoza, A.; Zhao, Y. Optimal energy transfer in light-harvesting systems. *Molecules.* **2015**, *20*, 15224-15272.

(4) Cao, J. S.; Cogdell, R. J.; Coker, D. F.; Duan, H. G.; Hauer, J.; Kleinekathöfer, U.;

Jansen, T. L. C.; Mancăl, T.; Miller, R. J. D.; Ogilvie, J. P.; Prokhorenko, V. I.; Renger, T.; Tan, H. S.; Tempelaar, R.; Thorwart, M.; Thyrhaug, E.; Westenhoff, S.; Zigmantas, D. Quantum biology revisited. *Sci. Adv.* **2020**, *6*, eaaz4888.

(5) Cho, M. *Two-dimensional Optical Spectroscopy*; CRC Press: New York, 2009.

(6) Hamm, P.; Zanni, M. *Concepts and Methods of 2D Infrared spectroscopy*; Cambridge University Press: Cambridge, 2011.

(7) Mukamel, S. *Principles of Nonlinear Optical Spectroscopy*; Oxford University Press: New York, 1995.

(8) Gelin, M. F.; Egorova, D.; Domcke, W. Efficient Calculation of Time- and Frequency-Resolved Four-Wave-Mixing Signals. *Acc. Chem. Res.* **2009**, *42*, 1290-1298.

(9) Seidner, L.; Stock, G.; Domcke, W. Nonperturbative approach to femtosecond spectroscopy: General theory and application to multidimensional nonadiabatic photoisomerization processes. *J. Chem. Phys.* **1995**, *103*, 3998-4011.

(10) Domcke, W.; Stock, G. Theory of ultrafast nonadiabatic excited-state processes and their spectroscopic detection in real time. *Adv. Chem. Phys.* **1997**, *100*, 1-169.

(11) Wang, H. B.; Thoss, M. Nonperturbative quantum simulation of time-resolved nonlinear spectra: Methodology and application to electron transfer reactions in the condensed phase. *Chem. Phys.* **2008**, *347*, 139-151.

(12) Brüggemann, B.; Persson, P.; Meyer, H. D; May, V. Frequency dispersed transient absorption spectra of dissolved perylene: A case study using the density matrix version of the MCTDH method. *Chem. Phys.* **2008**, *347*, 152-165.

(13) Gao, X.; Geva, E. A Nonperturbative Methodology for Simulating Multidimensional Spectra of Multiexcitonic Molecular Systems via Quasiclassical Mapping Hamiltonian Methods. *J. Chem. Theory Comput.* **2020**, *16*, 6491-6502.

(14) Gelin, M. F.; Egorova, D.; Domcke, W. Efficient calculation of the polarization induced by N coherent laser pulses. *J. Chem. Phys.* **2009**, *131*, 194103.

(15) Tanimura, Y. Stochastic Liouville, Langevin, Fokker-Planck, and master equation approaches to quantum dissipative systems. *J. Phys. Soc. Jpn.* **2006**, *75*, 082001.

(16) Tanimura, Y. Numerically "exact" approach to open quantum dynamics: The hierarchical equations of motion (HEOM). *J. Chem. Phys.* **2020**, *153*, 020901.

(17) Makri, N.; Makarov, D. E. Tensor propagator for iterative quantum time evolution of reduced density matrices. I. Theory. *J. Chem. Phys.* **1995**, *102*, 4600-4610.

(18) Makri, N.; Makarov, D. E. Tensor propagator for iterative quantum time evolution of reduced density matrices. II. Numerical methodology. *J. Chem. Phys.* **1995**, *102*, 4611-4618.

(19) Tanimura, Y.; Ishizaki, A. Modeling, Calculating, and Analyzing Multidimensional Vibrational Spectroscopy. *Acc. Chem. Res.* **2009**, *42*, 1270-1279.

(20) Tanimura, Y. Reduced hierarchy equations of motion approach with Drude plus Brownian spectral distribution: Probing electron transfer processes by means of two-dimensional correlation spectroscopy. *J. Chem. Phys.* **2012**, *137*, 22A550.

(21) Ikeda, T.; Tanimura, Y. Probing photoisomerization processes by means of multidimensional electronic spectroscopy: The multi-state quantum hierarchical Fokker-Planck equation approach. *J. Chem. Phys.* **2017**, *147*, 014102.

(22) Liang, X. T. Simulating signatures of two-dimensional electronic spectra of the Fenna-Matthews-Olson complex: By using a numerical path integral. *J. Chem. Phys.* **2014**, *141*, 044116.

(23) Hu, J.; Luo, M.; Jiang, F.; Xu, R. X.; Yan, Y. J. Padé spectrum decompositions of

quantum distribution functions and optimal hierarchical equations of motion construction for quantum open systems. *J. Chem. Phys.* **2011**, *134*, 244106.

(24) Tang, Z.; Ouyang, X. Q.; Gong, Z.; Wang, H.; Wu, J. L. Extended hierarchy equations of motion for the spin-boson model. *J. Chem. Phys.* **2015**, *143*, 224112.

(25) Rahman, H.; Kleinekathöfer, U. Chebyshev hierarchical equations of motion for systems with arbitrary spectral densities and temperatures. *J. Chem. Phys.* **2019**, *150*, 244104.

(26) Breuer, H. P.; Petruccione, F. *The Theory of Open Quantum Systems*; Oxford University Press: New York, 2007.

(27) Jang, S. J.; Mennucci, B. Delocalized excitons in natural light-harvesting complexes. *Rev. Mod. Phys.* **2018**, *90*, 035003.

(28) Yang, M.; Fleming, G. R. Influence of phonons on exciton transfer dynamics: comparison of the Redfield, Förster, and modified Redfield equations. *Chem. Phys.* **2002**, *282*, 163-180.

(29) Meier, C.; Tannor, D. J. Non-Markovian evolution of the density operator in the presence of strong laser fields. *J. Chem. Phys.* **1999**, *111*, 3365.

(30) Jang, S.; Cheng, Y. C.; Reichman, D. R.; Eaves, J. D. Theory of coherent resonance energy transfer. *J. Chem. Phys.* **2008**, *129*, 101104.

(31) McCutcheon, D. P. S.; Nazir, A. Consistent treatment of coherent and incoherent energy transfer dynamics using a variational master equation. *J. Chem. Phys.* **2011**, *135*, 114501.

(32) Shi, Q.; Geva, E. A semiclassical generalized quantum master equation for an arbitrary system-bath coupling. *J. Chem. Phys.* **2004**, *120*, 10647.

(33) Smith, J. I.; Dijkstra, A. G.; Lambert, N.; Nazir, A. Energy transfer in structured and unstructured environments: Master equations beyond the Born-Markov approximations. *J. Chem. Phys.* **2016**, 144, 044110.

(34) Beck, M. H.; Jäckle, A.; Worth, G. A.; Meyer, H. D. The Multiconfiguration Time-Dependent Hartree (MCTDH) Method: A Highly Efficient Algorithm for Propagating Wavepackets. *Phys. Rep.* **2000**, *324*, 1-105.

(35) Worth, G. A.; Meyer, H. D.; Köppel, H.; Cederbaum, L. S.; Burghardt, I. Using the MCTDH Wavepacket Propagation Method to Describe Multimode Non-Adiabatic Dynamics. *Int. Rev. Phys. Chem.* **2008**, *27*, 569-606.

(36) Wang, H. B.; Thoss, M. Multilayer formulation of the multiconfiguration time-dependent Hartree theory. *J. Chem. Phys.* **2003**, *119*, 1289.

(37) Manthe, U. A multilayer multiconfigurational time-dependent Hartree approach for quantum dynamics on general potential energy surfaces. *J. Chem. Phys.* **2008**, *128*, 164116.

(38) Ben-Nun, M.; Martínez, T. J. Nonadiabatic Molecular Dynamics: Validation of the Multiple Spawning Method for a Multidimensional Problem. *J. Chem. Phys.* **1998**, *108*, 7244-7257.

(39) Ben-Nun, M.; Martínez, T. J. A multiple spawning approach to tunneling dynamics. *J. Chem. Phys.* **2000**, *112*, 6113.

(40) Shalashilin, D. V.; Child, M. S. The Phase Space CCS Approach to Quantum and Semiclassical Molecular Dynamics for High-dimensional System. *Chem. Phys.* **2004**, *304*, 103-120.

(41) Shalashilin, D. V. Quantum mechanics with the basis set guided by Ehrenfest trajectories: Theory and application to spin-boson model. *J. Chem. Phys.* **2009**, *130*, 244101.

(42) Shalashilin, D. V. Nonadiabatic dynamics with the help of multiconfigurational Ehrenfest method: Improved theory and fully quantum 24D simulation of pyrazine. *J. Chem. Phys.* **2010**, *132*, 244111.

(43) Chen, L. P.; Gelin, M. F.; Shalashilin, D. V. Dynamics of a one-dimensional Holstein polaron: The multiconfigurational Ehrenfest method. *J. Chem. Phys.* **2019**, *151*, 244116.

(44) Richings, G. W.; Polyak, I.; Spinlove, K. E.; Worth, G. A.; Burghardt, I.; Lasorne, B. Quantum dynamics simulations using Gaussian wavepackets; the vMCG method. *Int. Rev. Phys. Chem.* **2015**, *34*, 269-308.

(45) Deng, T.; Yan, Y.; Chen, L.; Zhao, Y. Dynamics of the two-spin spin-boson model with a common bath. *J. Chem. Phys.* **2016**, *144*, 144102.

(46) Chen, L.; Borrelli, R.; Zhao, Y. Dynamics of Coupled Electron-Boson Systems with the Multiple Davydov D_1 Ansatz and the Generalized Coherent State. *J. Phys. Chem. A.* **2017**, *121*, 8757-8770.

(47) Chen, L.; Gelin, M. F.; Zhao, Y. Dynamics of the spin-boson model: A comparison of the multiple Davydov D_1, $D_{1.5}$, D_2 Ansätze. *Chem. Phys.* **2018**, *515*, 108-118.

(48) Chen, L.; Gelin, M. F.; Domcke, W. Multimode quantum dynamics with multiple Davydov D_2 trial states: Application to a 24-dimensional conical intersection model. *J. Chem. Phys.* **2019**, *150*, 024101.

(49) Zhou, N.; Chen, L.; Huang, Z.; Sun, K.; Tanimura, Y.; Zhao, Y. Fast, Accurate Simulation of Polaron Dynamics and Multidimensional Spectroscopy by Multiple Davydov Trial State. *J. Phys. Chem. A.* **2016**, *120*, 1562-1576.

(50) Huynh, T.; Sun, K.; Gelin, M. F.; Zhao, Y. Polaron dynamics in two-dimensional photon-echo spectroscopy of molecular rings. *J. Chem. Phys.* **2013**, *139*, 104103.

(51) Burghardt, I.; Nest, M.; Worth, G. A. Multiconfigurational System-bath Dynamics Using Gaussian Wavepackets; Energy Relaxation and Decoherence Induced by a Finite-dimensional Bath. *J. Chem. Phys.* **2003**, *119*, 5364.

(52) Burghardt, I.; Giri, K.; Worth, G. A. Multimode Quantum Dynamics Using Gaussian Wavepackets: The Gaussian-based Multiconfiguration Time-dependent Hartree (G-MCTDH) Method Applied to the Absorption Spectrum of Pyrazine. *J. Chem. Phys.* **2008**, *129*, 174104.

(53) Wang, L.; Fujihashi, Y.; Chen, L. P.; Zhao, Y. Finite-temperature time-dependent variation with multiple Davydov states. *J. Chem. Phys.* **2017**, *146*, 124127.

(54) Werther, M.; Choudhury, S. L.; Grossmann, F. Coherent state based solutions of the time-dependent Schrödinger equation: hierarchy of approximations to the variational principle. *Int. Rev. Phys. Chem.* **2021**, *40*, 81-125.

(55) Suzuki, M. Thermo Field Dynamics in Equilibrium and Non-Equilibrium Interacting Quantum Systems. *J. Phys. Soc. Jpn.* **1985**, *54*, 4483-4485.

(56) Takahashi, Y.; Umezawa, H. Thermo Field Dynamics. *Int. J. Mod. Phys. B.* **1996**, *10*, 1755-1805.

(57) Borrelli, R.; Gelin, M. F. Quantum electron-vibrational dynamics at finite temperature: Thermo field dynamics approach. *J. Chem. Phys.* **2016**, *145*, 224101.

(58) Borrelli, R.; Gelin, M. F. Simulation of Quantum Dynamics of Excitonic Systems at Finite Temperature: an efficient method based on Thermo Field Dynamics. *Sci. Rep.* **2017**, *7*, 9127.

(59) Chen, L. P.; Zhao, Y. Finite temperature dynamics of a Holstein polaron: The thermo-field dynamics approach. *J. Chem. Phys.* **2017**, *147*, 214102.

(60) Reddy, C. S.; Prasad, M. D. Finite temperature vibronic spectra of harmonic surfaces: a time-dependent coupled cluster approach. *Mol. Phys.* **2015**, *113*, 3023-3030.

(61) Begušić, T.; Vaníček, J. On-the-fly ab initio semiclassical evaluation of vibronic spectra at finite temperature. *J. Chem. Phys.* **2020**, *153*, 024105.

(62) Harsha, G.; Henderson, T. M.; Scuseria, G. E. Thermofield theory for finite-temperature quantum chemistry. *J. Chem. Phys.* **2019**, *150*, 154109.

(63) Harsha, G.; Henderson, T. M.; Scuseria, G. E. Thermofield Theory for Finite-Temperature Coupled Cluster. *J. Chem. Theory. Comput.* **2019**, *15*, 6127-6136.

(64) Chen, L. P.; Sun, K. W.; Shalashilin, D. V.; Gelin, M. F.; Zhao, Y. Efficient simulation of time- and frequency-resolved four-wave-mixing signals with a Multiconfigurational Ehrenfest approach. *J. Chem. Phys.* **2021**, *154*, 054105.

(65) Miyata, K.; Kurashige, Y.; Watanabe, K.; Sugimoto, T.; Takahashi, S.; Tanaka, S.; Takeya, J.; Yanai, T.; Matsumoto, Y. Coherent singlet fission activated by symmetry breaking. *Nat. Chem.* **2017**, *9*, 983-989.

(66) Sun, K. W.; Huang, Z. K.; Gelin, M. F.; Chen, L. P.; Zhao, Y. Monitoring of singlet fission via two-dimensional photon-echo and transient-absorption spectroscopy: Simulations by multiple Davydov trial states. *J. Chem. Phys.* **2019**, *151*, 114102.

(67) Hu, W. J.; Sun, K. W.; Xu, Q.; Chen, L. P.; Zhao, Y. Ultrafast dynamics in rubrene and its spectroscopic manifestation. *J. Chem. Phys.* **2020**, *153*, 174105.

(68) Sun, K. W.; Xu, Q.; Chen, L. P.; Gelin, M. F.; Zhao, Y. Temperature effects on singlet fission dynamics mediated by a conical intersection. *J. Chem. Phys.* **2020**, *153*, 194106.

(69) Makri, N. The Linear Response Approximation and Its Lowest Order Corrections: An Influence Functional Approach. *J. Phys. Chem. B.* **1999**, *103*, 2823-2829.

(70) Wang, H.; Thoss, M.; Miller, W. H. Systematic convergence in the dynamical hybrid approach for complex systems: A numerically exact methodology. *J. Chem. Phys.* **2001**, *115*, 2979.

(71) Bramley, O.; Symonds, C.; Shalashilin, D. V. Quantum system-bath dynamics with

quantum superposition sampling and coupled generalized coherent states. *J. Chem. Phys.* **2019**, *151*, 064103.

(72) Shalashilin, D. V.; Child, M. S. Basis set sampling in the method of coupled coherent states: Coherent state swarms, trains, and pancakes. *J. Chem. Phys.* **2008**, *128*, 054102.

(73) Gelin, M. F.; Pisliakov, A. V.; Domcke, W. Time- and frequency-gated spontaneous emission as a tool for studying vibrational dynamics in the excited state. *Phys. Rev. A.* **2002**, *65*, 062507.

(74) Egorova, D.; Gelin, M. F.; Domcke, W. Time- and frequency-resolved fluorescence spectra of nonadiabatic dissipative systems: What photons can tell us. *J. Chem. Phys.* **2005**, *122*, 134504.

(75) Chen, L. P.; Gelin, M. F.; Zhao, Y.; Domcke, W. Mapping of Wave Packet Dynamics at Conical Intersections by Time- and Frequency-Resolved Fluorescence Spectroscopy: A Computational Study. *J. Phys. Chem. Lett.* **2019**, *10*, 5873-5880.

(76) Sun, K. W.; Xie, W. W.; Chen, L. P.; Domcke, W.; Gelin, M. F. Multi-faceted spectroscopic mapping of ultrafast nonadiabatic dynamics near conical intersections: A computational study. *J. Chem. Phys.* **2020**, *153*, 174111.

(77) Bakulin, A. A.; Morgan, S. E.; Kehoe, T. B.; Wilson, M. W. B.; Chin, A. W.; Zigmantas, D.; Egorova, D.; Rao, A. Real-time observation of multiexcitonic states in ultrafast singlet fission using coherent 2D electronic spectroscopy. *Nat. Chem.* **2016**, *8*, 16-23.

(78) Makhov, D.; Glover, W. J.; Martínez, T. J.; Shalashilin, D. V. Ab initio Multiple cloning algorithm for quantum nonadiabatic molecular dynamics. *J. Chem. Phys.* **2014**, *141*, 054110.

(79) Makhov, D.; Symonds, C.; Alberti, S. F.; Shalashilin, D. V. Ab initio quantum direct

dynamics simulations of ultrafast photochemistry with Multiconfigurational Ehrenfest approach. *Chem. Phys.* **2017**, *493*, 200-218.

Graphical TOC Entry